

This is an Open Access document downloaded from ORCA, Cardiff University's institutional repository: <https://orca.cardiff.ac.uk/id/eprint/135361/>

This is the author's version of a work that was submitted to / accepted for publication.

Citation for final published version:

Lambert-Smith, James S. , Allibone, Andrew, Treloar, Peter J., Lawrence, David M., Boyce, Adrian J. and Fanning, Mark 2020. Stable C, O, and S isotope record of magmatic-hydrothermal interactions between the Falémé Fe Skarn and the Loulo Au systems in Western Mali. *Economic Geology* 115 (7) 10.5382/econgeo.4759

Publishers page: <http://dx.doi.org/10.5382/econgeo.4759>

Please note:

Changes made as a result of publishing processes such as copy-editing, formatting and page numbers may not be reflected in this version. For the definitive version of this publication, please refer to the published source. You are advised to consult the publisher's version if you wish to cite this paper.

This version is being made available in accordance with publisher policies. See <http://orca.cf.ac.uk/policies.html> for usage policies. Copyright and moral rights for publications made available in ORCA are retained by the copyright holders.



1 **Stable C, O and S Isotope Record of Magmatic-Hydrothermal Interactions**
2 **Between the Falémé Fe Skarn and the Loulo Au Systems in Western Mali**

3 **James S. Lambert-Smith^{1*}, Andrew Allibone², Peter J. Treloar³, David M. Lawrence²,**
4 **Adrian J. Boyce⁴, Mark Fanning⁵**

5 ¹School of Earth and Ocean Sciences, Cardiff University, Main Building, Park Place, Cardiff, CF10 3AT,
6 UK

7 ²Barrick Gold (Holdings) Ltd, 3rd Floor, Unity Chambers, 28 Halkett St., St Helier, Jersey JE2 4WJ,
8 Channel Islands, UK

9 ³School of Natural and Built Environments, Kingston University London, Kingston upon Thames, KT1
10 2EE

11 ⁴Scottish Universities Environmental Research Centre, East Kilbride, Glasgow, Scotland, G75 0QF

12 ⁵Research School of Earth Sciences, Australian National University, Canberra ACT0200, Australia

13 *Corresponding author email address: lambert-smithj@cardiff.ac.uk

14 **Keywords:** Stable isotopes; Loulo Mining District; Birimian; Orogenic gold mineralization; Iron skarns

15 **Abstract**

16 The Gara, Yalea and Goukoto Au deposits of the 17+ Moz Loulo Mining District, largely hosted by
17 the Kofi Series metasediments, are located several kms to the east of the 650 Mt Fe skarn deposits in
18 the adjacent Falémé Batholith. The Au deposits are interpreted to have formed through phase separation
19 of an aqueous-carbonic fluid, which locally mixed with a hypersaline brine of meta-evaporite origin.
20 Recognition of an intrusive relationship between the Falémé Batholith and Kofi Series opens the
21 possibility that the Fe skarns and Au deposits are part of the same mineral system. In this paper, we
22 combine new $\delta^{13}\text{C}$, $\delta^{18}\text{O}$ and $\delta^{34}\text{S}$ data from the Karakaene Ndi skarn, minor Au occurrences along the
23 western margin of the Kofi Series, and zircons within plutonic rocks of the Falémé Batholith with
24 existing data from the Loulo Au deposits, to model the contribution of magmatic volatiles to Au
25 mineralization.

26 C- and O-isotope compositions of auriferous carbonate-quartz-sulfide veins from the Loulo Au deposits
27 have wide ranges ($\delta^{13}\text{C}$: -21.7 to -4.5 ‰ and $\delta^{18}\text{O}$: 11.8 to 23.2 ‰), whereas values from carbonate
28 veins in Kofi Series Au prospects close to the Falémé Batholith, and the Karakaene Ndi Fe skarn
29 deposit, have more restricted ranges ($\delta^{13}\text{C}$: -16.8 to -3.7 ‰, $\delta^{18}\text{O}$: 11.4 to 17.2 ‰ and $\delta^{13}\text{C}$ -3.0 ± 1 ‰,
30 $\delta^{18}\text{O}$ 12.6 ± 1 ‰, respectively). Kofi Series dolostones have generally higher isotopic values ($\delta^{13}\text{C}$: -
31 3.1 to 1.3 ‰ and $\delta^{18}\text{O}$: 19.1 to 23.3 ‰). Pyrite from Kofi Series Au prospects adjacent to the Falémé

32 Batholith, have a wide range of $\delta^{34}\text{S}$ values (−4.6 to 14.2 ‰), similar to pyrite from the Karakaene Ndi
33 skarn (2.8 to 11.9 ‰), whereas $\delta^{34}\text{S}$ values of pyrite and arsenopyrite from the Loulo deposits are
34 consistently > 6 ‰.

35 Comparison of the C- and O-isotopic data with water-rock reaction models indicates the Loulo Au
36 deposits formed primarily through unmixing of an aqueous carbonic fluid derived from the
37 devolatilisation of sedimentary rocks with an organic carbon component. Isotopic data are permissive
38 of the hypersaline brine which enhanced this phase separation including components derived from both
39 Kofi Series evaporite horizons interlayered with the dolostones and a magmatic-hydrothermal brine.
40 This magmatic-hydrothermal component is particularly apparent in O-, C-, and S-isotopic data from the
41 Gara deposit and Au prospects immediately adjacent to the Falémé Batholith.

43 Orogenic deposits account for ~30 % of total Au production, reserves, and resources (Frimmel and
44 Hennigh, 2015), making them one of the most important sources of Au globally. Most of these deposits
45 formed from near neutral low salinity aqueous-carbonic fluids at temperatures between 250-400°C in
46 greenschist facies metamorphic terranes (e.g. Groves et al., 1998; Goldfarb et al., 2005; Phillips and
47 Powell, 2010; Goldfarb and Groves, 2015). There is widespread consensus that metasedimentary and /
48 or metabasaltic rocks undergoing metamorphic devolatilization reactions are the ultimate source of the
49 ore fluids in orogenic gold deposits, with the metals scavenged from the same rocks (Henley et al.,
50 1976; Norris and Henley, 1976; Kerrich and Wyman, 1990; Goldfarb et al., 1991; Phillips and Powell,
51 1993; McCuaig and Kerrich, 1998; Pitcairn et al., 2006, Gaboury, 2013; Tomkins, 2013; Pitcairn et al.,
52 2014; Yardley and Cleverley, 2015; Goldfarb and Groves, 2015; Wyman et al., 2016; Groves et al.,
53 2019). However, speculation remains that some deposits include hydrothermal fluids exsolved from
54 crystallizing magmas (Lawrence et al., 2013a, 2013b; Xue et al., 2013; Treloar et al., 2015; Spence-
55 Jones et al., 2018). Resolving this question is an important part of the development of a holistic mineral
56 system model for orogenic Au deposits (Wyman et al., 2016; Groves et al., 2019).

57 The 17+ Moz Loulo Au Mining District in the Kédougou-Kéniéba inlier in western Mali and eastern
58 Senegal is one of the most richly endowed orogenic Au districts in the West Africa craton (Fig. 1). It
59 includes three major multi-million ounce deposits, including Gara, Yalea, and Goukoto and numerous
60 satellite deposits that typically contain <1 Moz Au (e.g., Baboto, Faraba, Loulo 3, Loulo 2, P64, and
61 P129). Small-displacement, discontinuous shear-zones, some of which may have nucleated along earlier
62 fold axial planes. Quartz-tourmaline-altered quartz gritstone units within the Kofi Series siliciclastic,
63 carbonate, and evaporitic rocks host the Au deposits. The western margin of the Kofi Series is intruded
64 and unconformably overlain by high-K plutonic rocks of the Falémé Batholith and related Bambadji
65 Formation volcanic rocks, respectively. Magnetite and hematite-rich endoskarns, which contain > 650
66 Mt Fe, are present within the Falémé Batholith. Related exoskarns locally extend into the Bambadji
67 Formation and the western-most parts of the Kofi Series, further demonstrating the intrusive
68 relationship between the Falémé Batholith and Kofi Series at the time skarn mineralization occurred.

69 Despite several detailed studies of the Au deposits (Fouillac et al., 1993; Lawrence et al., 2013a;
70 Lawrence et al., 2013b; Lambert-Smith et al., 2016b; Lambert-Smith et al., 2016c), the ultimate source
71 of fluids and Au in the Loulo mineral system remains uncertain. Lawrence et al. (2013b) proposed a
72 magmatic contribution to auriferous fluids due to the presence of a high-temperature (>400 °C)
73 hypersaline brine in several deposits. However, Lambert-Smith et al. (2016b) argued against a
74 magmatic source for the brines on the basis of B, S, C, and O isotopic data. In particular, B-isotope data
75 indicate derivation of brines from evaporite units in the Kofi Series (Lambert-Smith et al., 2016c).
76 Nevertheless, the Falémé Batholith and associated skarns intrude and extend into the Kofi Series,

77 instead of being separated by a terrane boundary (Senegal-Mali Shear Zone), reopens the possibility
78 that the Falémé Fe magmatic-hydrothermal system contributed to Au mineralization at Loulo.
79 Furthermore, Masurel et al. (2017c) report direct overprinting of calc-silicate skarn mineralization by
80 biotite-calcite-quartz \pm K-feldspar-tourmaline-actinolite alteration associated with Au mineralisation at
81 the Sadiola Hill Au deposit. The deposit is carbonate-hosted and located in the northern part of the
82 Kédougou-Kéniéba inlier in the vicinity of an intrusive centre correlative with the Falémé Batholith.

83 The Baqata, Kolya, Kabe West and Gefa (Fig. 2) prospects are hosted in the Kofi Series, less than 2 km
84 from the intrusive contact with the Falémé Batholith. Minor Au-bearing veins are also present within
85 the Falémé Batholith, at the Boboti target. These Au occurrences, within the batholith and midway
86 between the batholith margin and major Au deposits of the Loulo Mining District, provide an
87 opportunity to examine the genetic links between the Falémé Fe skarns (Schwartz and Melcher, 2004)
88 and the Loulo Au deposits. Furthermore, samples from the Karakaene Ndi Fe skarn deposits provide
89 data on the isotopic character of the Fe skarns and any local magmatic-hydrothermal contribution to the
90 Au deposits. Here we use new C, O and S isotope data from these Au occurrences and from the
91 Karakaene Ndi skarn, together with existing isotopic data from Gara, Yalea and Goukoto (Fouillac et
92 al., 1993; Lawrence et al., 2013b; Lambert-Smith et al., 2016b), as tracers for the source to ore pathways
93 of auriferous fluids. The magmatic contribution, if any, to Au mineralization in the Kofi Series is based
94 on new Sensitive High-Resolution Ion Microprobe (SHRIMP) $\delta^{18}\text{O}$ analyses of magmatic zircons
95 recovered from the Falémé Batholith.

96

Geological Setting

97 The 2.27 to 2.05 Ga Paleoproterozoic terranes of the southern West African Craton constitute one of
98 the world's leading Au-provinces, with an overall endowment in excess of 350 Moz (Goldfarb et al.,
99 2017; Thebaud et al., in press). Paleoproterozoic rocks are exposed in the Baoulé-Mossi domain, the
100 Kédougou-Kéniéba and Kayes inliers (Fig. 1), and in the eastern Reguibat Rise in North Africa. They
101 include shear-bounded, linear and arcuate belts of volcano-sedimentary rocks ca. 2270-2150 Ma old
102 (e.g. Baratoux et al., 2011), younger sedimentary basins ca. 2135-2095 Ma old (e.g. Taylor et al., 1992;
103 Lebrun et al., 2015), and granitoid-dominated terranes ca. 2190-2060 Ma old (e.g. Hirdes et al., 1992;
104 Parra-Avila et al., 2017) . The volcano-sedimentary belts largely comprise lavas of tholeiitic and calc-
105 alkaline affinity, volcanoclastic rocks, and epiclastic sedimentary rocks. The basins are filled with
106 siliciclastic rocks, including arkoses, greywackes, argillites, arenites, and rare limestones and chemical
107 sediments. Multiple suites of granitoid rocks intrude both the belts and the basins.

108 The Paleoproterozoic terranes formed, accreted, and were deformed over \sim 200 Myr (e.g. Perrouty et
109 al., 2012; White et al., 2014; Parra-Avila et al., 2016; Grenholm et al., 2019; Thebaud in press) during
110 the 2266-2140 Ma Eoeburnean , and 2135-2050 Ma Eburnean periods (e.g. Taylor et al., 1992; Dia et
111 al., 1997; Loh et al., 2000; Allibone et al., 2002; Gueye et al., 2007; Hein, 2010; De Kock et al., 2011;

112 Baratoux et al., 2011; Tshibubudze et al., 2015). Initial volcanism, granitoid emplacement, fold and
113 thrust tectonics, and metamorphism took place during Eoeburnean crustal growth and accretion. The
114 ages of the youngest detrital zircon populations indicate that the sedimentary basins developed from
115 2135 to 2095 Ma (Davis et al., 1994; Oberthür et al., 1998; Hirdes and Davis, 2002; Vidal et al., 2009;
116 Lebrun et al., 2016). Emplacement of younger granitoid plutons (Parra-Avila et al., 2018; Masurel et
117 al., 2017a), further contractional deformation and metamorphism, late strike-slip deformation, and
118 widespread Au mineralization occurred during the subsequent Eburnean orogeny (Oberthür et al., 1998;
119 McFarlane et al., 2011; Parra-Avila et al., 2015; Fontaine et al., 2017; Fougrouse et al., 2017; Masurel
120 et al., 2017b). Greenschist facies mineral assemblages dominate in most Paleoproterozoic rocks across
121 West Africa, but amphibolite and granulite facies assemblages are present locally within both the
122 Eoeburnean belts and Eburnean sedimentary basins (John et al., 1999; White et al., 2014; MacFarlane
123 et al., 2019). Particularly low geothermal gradients of 10-12° C km⁻¹ are consistent with modern
124 subduction processes during Eburnean time in some parts of the craton (Ganne et al., 2011; Block et al.
125 2015).

126

Geology of the Loulo Mining District

127 The Kofi Series comprises metamorphosed immature detrital sedimentary and carbonate rocks
128 deposited after 2120-2100 Ma. The former are dominantly sandstones, wackes, and argillites that
129 include both quartz- and feldspar-rich siliciclastic components. Carbonate lithologies are more abundant
130 in the west, close to the contact with the Falémé Batholith (Fig. 2). These are dominantly dolomitic,
131 with mm to cm-scale marl horizons that contain clasts of fine-grained, sub-angular quartz and feldspar
132 and very fine-grained muscovite. Carbonate lithologies also contain a minor graphitic-argillaceous
133 component, present as mm to sub-mm scale lamellae, or as fine rounded and strained clasts. The Kofi
134 Series sedimentary rocks were tilted upright, tightly folded, cut by reverse faults, and metamorphosed
135 under upper greenschist facies biotite zone conditions during D₁ contractional deformation between ca.
136 2100-2090 Ma. Later small-scale (< 1 km) folding and development of an associated steeply dipping
137 axial planar cleavage, and Au mineralization occurred during D₂ sinistral transcurrent deformation
138 between ca. 2085 and 2060 Ma (Hirdes and Davis, 2002; Schwartz and Melcher, 2004; Lawrence et al.,
139 2013a; Masurel et al., 2017a; Masurel et al., 2017b). The Falémé Batholith, and associated outlying
140 plutons and dikes, intruded the Kofi Series between 2084 ± 8 Ma and 2075 ± 6 Ma, after inversion of
141 the Kofi Series during D₁ contraction. Outlying dikes of the Falémé batholith at Goukoto and Gara
142 have been affected by the later stages of hydrothermal activity and syn-Au deformation indicating
143 magmatism occurred during the earlier stage(s) of D₂, prior to mineralisation, but nevertheless part of
144 the same overall D₂ event. While the exact timing of mineralization is yet to be determined, these
145 relationships suggest magmatic activity and Au mineralization were broadly synchronous.

146 Lawrence et al. (2013a, b) describe two end-member styles of Au mineralization at Loulo, termed Gara-
147 and Yalea-style, respectively. Gara-style deposits are characterized by pyrite dominated ores with metal
148 signatures enriched in Fe-Rare Earth Element (REE)-W and rare base metals. Intense tourmaline
149 alteration, which is atypical of orogenic Au deposits (e.g. Groves et al., 1998), and hypersaline fluid
150 inclusions further characterise this style of mineralization (Lawrence et al., 2013b). Conversely, Yalea-
151 style deposits are As-rich and lack REE and base metal enrichment. Alteration assemblages consist of
152 early quartz-carbonate-albite, overprinted by sericite-chlorite-sulfide-Au (Lawrence et al., 2013a).
153 Fluids are dilute and aqueous-carbonic in character (Lawrence et al., 2013b). The Goukoto deposit
154 exhibits characteristics in common with both styles, including hypersaline fluid inclusions and As-rich
155 sulfide assemblages (Lambert-Smith et al., 2016b). Satellite deposits and exploration targets in the
156 region display characteristics of either style (Lawrence et al., 2013a; Lambert-Smith, 2014a). All Au
157 and Fe mineralization in the district is associated with moderate to intense albitization, which affects
158 most rock types.

159 Lawrence et al. (2013b) interpreted fluid inclusion assemblages as representing two distinct end-
160 member fluids: 1) a high T, high-salinity, CO₂-poor, aqueous fluid (~400°C; ~45-55 wt. % NaCl equiv.);
161 and 2) a moderate T, dilute, aqueous-carbonic fluid (270-350°C; <10 wt. % NaCl equiv.). Partial mixing
162 between these fluids at Gara-style ore bodies resulted in retrograde boiling and changes in the
163 physicochemical state of both fluids leading to sulfide mineralization and Au precipitation (Lawrence
164 et al., 2013a, b). At Yalea, the hypersaline fluid is absent and fluid inclusion assemblages feature two
165 immiscible phases derived from phase separation of a dilute aqueous-carbonic fluid (Lawrence et al.,
166 2013b). This likely occurred in response to a combination of fluid-rock interaction, particularly
167 sulfidation, and pressure fluctuations along the brittle-ductile host structures. Stable isotope data from
168 Au-related quartz ($\delta^{18}\text{O}$ from 12.9 to 17.4 ‰), dolomite ($\delta^{13}\text{C}$ from -21.7 to -4.5 ‰), and pyrite ($\delta^{34}\text{S}$
169 from 5.8 to 15.5 ‰) (Lawrence et al., 2013b) at Gara, Yalea and Goukoto are generally consistent
170 with fluids being sourced from the devolatilization of Kofi Series metasedimentary rocks (Lambert-
171 Smith et al., 2016b), though $\delta^{18}\text{O}$ and $\delta^{13}\text{C}$ values partially overlap magmatic fields. Furthermore, B-
172 isotope data from hydrothermal tourmaline indicates a meta-evaporite source for B, implying evaporite
173 devolatilization in the genesis of the hypersaline brine (Lambert-Smith et al., 2016c).

174 *Au and Fe mineralization in the western Kofi series and Falémé Batholith*

175 The minor Au occurrences along the western margin of the Kofi Series at Baqata, Kolya, Kabe West,
176 Boboti and Gefa (Fig. 2) have been described in detail by (Lambert-Smith, 2014a). The key geological
177 characteristics of these occurrences and the larger deposits are summarized in Table 1.

178 Baqata is located ~6.2 km SE of Goukoto (Fig. 2). Mineralization is hosted in a package of altered
179 Kofi Series quartz wacke, dolostone, and argillite interbedded with siltstones and sandstones, which
180 dips 60° W and strikes 185°. Bedding is cut by a sub-vertical NNE-striking cleavage which is axial

181 planar to 100 m-scale SSW plunging asymmetric F_2 folds. The sequence is intruded by 1-10 m thick,
182 variably albitized diorite and monzodiorite dikes, and cut by steeply dipping NNW-striking (80E/350)
183 shear zones. Mineralized rocks include both Gara-style ankerite-quartz-pyrite stockworks in
184 tourmalinized quartz wacke and disseminated pyrite and chlorite-pyrite stringers in albitized dolostone
185 and quartz wacke. Au grades locally reach 13.4 g/t but are discontinuous along strike and down-dip.
186 Like at Gara, accessory Ni-sulfides (e.g. millerite), xenotime, and monazite are present. Gold,
187 tellurobismuthite (Bi_2Te_3), calaverite and bismuth are occluded in pyrite and the gangue.

188 At Kolya, ~13 km south of Gara, discontinuous zones of mineralized rock that contain up to ~5.8 g/t
189 Au are hosted in a package of argillites, greywackes, tourmalinized quartz wackes, and dolostones,
190 which dips 70° W and strikes 350° . These rocks are folded, cleaved, and cut by shear zones in the same
191 manner as those at Baqata. Dolerite dikes intrude the sedimentary rock package. Mineralized rocks at
192 Kolya comprise chlorite-pyrite veins primarily within the dolerite dikes, and minor hydrothermal
193 breccias and ankerite-quartz-pyrite vein stockworks in tourmalinized quartz wacke. Gold occurs as
194 occluded grains and fracture-fill in pyrite and arsenian pyrite, where it is associated with minor altaite
195 (PbTe), melonite (NiTe_2) and tellurobismuthite. Kolya lacks Ni-sulfide phases.

196 Kabe West is located ~2.5 km south west of Kolya. Gold is hosted in intensely albitized igneous rocks
197 which intrude albitized dolostone, siliciclastic rocks and hydrothermal breccias. Gold grades are
198 typically 2-4 g/t (locally up to 11.3 g/t) and spatially discontinuous. Structural controls on
199 mineralization are not known due to poor exposure, lack of oriented drill core, and overprinting of pre-
200 mineralization fabrics by intense albitization. Pyrite is the dominant ore phase and contains up to 1.9
201 wt. % Co and 0.5 wt. % Ni. Gold, altaite and melonite occur as inclusions within, or annealed to, pyrite
202 grains, which are disseminated in albitized wall rock and in hydrothermal breccias with tourmaline or
203 dolomite cement.

204 Mineralized rocks at Gefa, ~7 km south of Baqata, are hosted in a package of albitized argillite,
205 dolostone, and greywacke. The host sedimentary rocks strike N-S and dip 80° W and are intruded by
206 unmineralized diorite and quartz feldspar porphyry dikes. These rocks are cut by sheared polymict
207 hydrothermal breccias. Mineralized rocks are generally characterized by Au grades < 0.5 g/t, localized
208 within zones of brittle quartz-carbonate-pyrite veining that cross cut intensely albitized rock.

209 Boboti is located ~8.3 km to the south west of Baqata. Mineralization is hosted in albitized subvolcanic
210 andesites and medium to coarse-grained diorites of the Boboti Pluton. Gold is hosted by pyrite grains
211 within carbonate-pyrite veinlets and minor disseminated pyrite in the immediate wall rock to veins.
212 Grades reach a maximum of 2.6 g/t Au, but mineralized zones are rarely continuous over more than 1
213 meter downhole.

214 The Falémé Iron District (Schwartz and Melcher 2004) endo- and exoskarn deposits are located within
215 the Falémé Batholith, associated altered Bambadji Formation volcanic rocks, and western-most parts
216 of the Kofi Series (Fig. 2). In the skarns, proximal halos of calc-silicate alteration (actinolite-epidote-
217 allanite-titanite \pm clinopyroxene-garnet) overprint regional albitization (Fig.3 a-e). This is further
218 overprinted by massive magnetite \pm apatite ore (Fig. 3f). Late sulfide mineralization which typically
219 includes coarse disseminated pyrite and chalcopyrite, or pyrite-chalcopyrite-calcite veins cuts the iron
220 ore (Fig. 3f, g). These sulfides are locally auriferous, typically containing < 0.5 g/t Au and rarely up to
221 3 g/t Au associated with trace amounts of Co-Ni-U-bearing phases. Preliminary fluid inclusion studies
222 by Schwartz and Melcher (2004) and Lambert-Smith (2014a) tentatively indicate a H₂O-NaCl-CO₂
223 magmatic fluid, with low salinity (approx. 3.3 wt. % NaCl equiv.) and XCO₂ = 0.11. The alteration and
224 ore mineralogy of the skarns share commonalities with Fe-oxide apatite deposits, and their close spatial
225 association with a large orogenic Au camp hints at IOCG affinities (Schwartz and Melcher 2004,
226 Lawrence et al. 2013a).

227

Sample characteristics and Methods

228 $\delta^{13}\text{C}$ and $\delta^{18}\text{O}$ was measured in 28 samples from the Kolya, Baqata, Boboti, Gefa and Kabe West
229 exploration targets and 7 samples from the Karakaene Ndi skarn (Fig. 2). These data include ankerite,
230 calcite and dolomite from auriferous, skarn-related, and barren hydrothermal veins and wall rock
231 alteration, and dolomite from host dolostone units (Fig. 4a). A further 49 $\delta^{13}\text{C}$ and $\delta^{18}\text{O}$ analyses are
232 included from published data for Goukoto (Lambert-Smith et al., 2016b); Gara (Fouillac et al., 1993 ;
233 Lawrence et al., 2013b), and Yalea (Lawrence et al., 2013b). $\delta^{34}\text{S}$ was measured in 23 pyrite samples
234 from Kolya, Baqata, Boboti and Kabe West exploration targets and in 11 pyrite samples from the
235 Karakaene Ndi skarn. Zircon $\delta^{18}\text{O}$ values were measured by SHRIMP on 3 samples of quartz
236 monzodiorite and quartz monzonite from the Falémé Batholith (RG10036, RG10039, RG10050) and
237 one sample of Bambadji Formation andesitic volcanoclastic rock (RG10030).

238 *Mineralized vein characteristics*

239 Tourmalinized quartz wacke units are important ore hosts at Gara and the P-64 satellite, subordinate
240 ore hosts at Goukoto, and host sub-economic mineralization at the Baqata and Kolya targets.
241 Tourmalinization involves the replacement of the matrices of wackes with cryptocrystalline tourmaline,
242 making the unit more brittle and therefore susceptible to the development of ankerite-quartz-pyrite-Au
243 \pm dolomite \pm tourmaline hydro fracture vein stockworks (Fig. 4b). These stockworks contain several
244 vein morphologies characteristic of the brittle-ductile environment, including planar centimeter- to
245 millimeter-scale veins and veinlets, brecciated and boudinaged veins, and sigmoidal vein arrays.
246 Veining is typically multi-generational, occurring in multiple orientations and at multiple scales (< 100
247 μm to $\sim 2\text{-}3$ cm vein width). This stockwork style of mineralization typically affects ~ 1 to 20 m thick

248 units and is associated with Au grades up to ~100 g/t. High grades are generally associated with strongly
249 altered host rocks, high carbonate and sulfide content in the veins, and the most intense vein networks
250 with several generations of veins. Veins at Gara commonly include late, gray, quartz-pyrite-Au cores
251 (Lawrence et al., 2013b).

252 In contrast, veining is a minor part of the mineralized rocks at Yalea and Goukoto, which include a
253 larger proportion of sulfide stringers, disseminations in the matrix of hydrothermal breccias, and
254 chloritic ductile shear zones. Mineralized veinlets at Yalea cross-cut ductile shear fabrics, and contain
255 arsenopyrite-pyrite-arsenian pyrite-Au \pm quartz \pm ankerite (Fig. 4c). At Goukoto quartz-carbonate-
256 pyrite-chlorite veins commonly occur several 10s of meters outside the main ore zone and are associated
257 with grades up to ~5 g/t Au. Veins are typically undeformed and may cross-cut earlier Au
258 mineralization. Mineralogically similar veins have been observed in high grade ore shoots but are
259 typically highly deformed and overprinted by later Au mineralization. Sulfides occupy up to 50 vol. %
260 of the vein assemblage (more typically ~20 %), and carbonate mineralogy is commonly dolomitic and
261 rarely ankeritic. Vein width varies from <100 μ m up to 6-7 cm. Many veins have been reactivated and
262 brecciated by later hydrothermal events. Undeformed hydrofracture veins and veinlets are also common
263 at the Baqata, Boboti, Gefa and Kabe West exploration targets.

264 At the Karakaene Ndi skarn, veining generally postdates the oxide ore. Veins are <1 mm to 6 cm thick
265 and composed of <100 μ m to >5 mm calcite-pyrite \pm quartz \pm chlorite \pm Au, with pyrite \approx calcite (Fig.
266 3g). Sulfide-rich veins do not show the zoned calc-silicate alteration halos characteristic of primary
267 oxide mineralization.

268 A small number of veins sampled from the Kofi Series were classified as mineralized based on the
269 presence of sulfide minerals, despite returning fire assay results below detection limit (<0.01 ppm).
270 These veins contain fine pyrite and chalcopyrite in variable abundance. Several of these veins contain
271 only one or two sub-mm-scale grains of pyrite or chalcopyrite (Fig. 4d), while others contain several
272 modal percent of coarse pyrite (some with multiple generations) (Fig. 4g).

273 *Barren vein characteristics*

274 Barren hydrothermal veining occurs throughout the Loulo Mining District (Fig. 4e-f). Pre-
275 mineralization barren quartz-carbonate veins are deformed and display asymmetric fold patterns (Fig.
276 4f). Late-stage barren quartz-carbonate veins, including at Gara, Yalea, and Goukoto, cross cut
277 mineralization and alteration (Lawrence et al., 2013a). Elsewhere in the district, similar veining cross
278 cuts barren country rock (Fig. 4e). These late veins are typically undeformed. The timing of veins
279 occurring outside the footprint of the large deposits is somewhat uncertain; it is possible that some of
280 these veins are barren equivalents to mineralized veins. The mineralogy in barren veins comprises

281 variable proportions of quartz-dolomite \pm chlorite, with no sulfide minerals present. Vein width ranges
282 from <1 mm to approximately 8 cm (typically <1 cm).

283 *Analytical procedures*

284 *Energy-dispersive X-ray spectroscopy* - Mineral compositions were determined using an Oxford
285 Instruments X-ACT Energy Dispersive System detector mounted on a Zeiss EVO 50 Scanning Electron
286 Microscope at Kingston University London. The EDS employed an accelerating voltage of 20 kV, a
287 beam current of 1.5 nA, and a detector process time of 4 seconds. The detection limit for all elements
288 was \sim 0.2 wt. %.

289 *Stable isotopes in carbonates and pyrite*- Carbon and oxygen isotopic analyses of carbonate minerals
290 were carried out at the Scottish Universities Environmental Research Centre (SUERC) in East Kilbride,
291 Scotland. CO₂ was liberated via *in vacuo* reaction with 100 % phosphoric acid at 100 °C for dolomite
292 and ankerite, and at 25 °C for calcite. The CO₂ was analysed on a VG SIRA 10 mass spectrometer. Data
293 were corrected using oxygen fractionation factors for acid-extracted CO₂ at 100 °C of 1.00913 and
294 1.00901 for dolomite and ankerite, respectively (Rosenbaum and Sheppard, 1986). CO₂ liberated at 25
295 °C from calcite was corrected using α of 1.0014 (Craig, 1957). Carbon and oxygen isotope data are
296 reported as per mill (‰) deviations relative to Vienna PeeDee belemnite (V-PDB) and Vienna Standard
297 Mean Ocean Water (V-SMOW), respectively. Lab reproducibility based on complete analysis of
298 internal standard MAB 2 (Carrara marble) and replicate analyses of calcite unknowns (including acid
299 digestion at 25 °C) was \pm 0.10 ‰ for $\delta^{13}\text{C}$ and \pm 0.12 ‰ for $\delta^{18}\text{O}$ (1 σ). Reproducibility based on repeat
300 analysis of dolomite unknowns (including acid digestion at 100 °C) was \pm 0.09 ‰ for $\delta^{13}\text{C}$ and \pm 0.10
301 ‰ for $\delta^{18}\text{O}$ (1 σ).

302 Pyrite separates were analysed by standard techniques (Robinson and Kusakabe, 1975). SO₂ gas was
303 liberated by combusting sulfides with excess Cu₂O at 1075 °C, *in vacuo*. Liberated SO₂ was analysed
304 on a VG Isotech SIRA II mass spectrometer, and standard corrections applied to raw $\delta^{66}\text{SO}_2$ values to
305 produce $\delta^{34}\text{S}$. The data were calibrated using international standards NBS-123 (Sharp, 2017) and IAEA-
306 S-3 (Mann et al., 2009), and the SUERC standard CP-1. Lab reproducibility was \pm 0.3 ‰ (1 σ). Data
307 are reported in $\delta^{34}\text{S}$ notation as per mil (‰) deviations from the Vienna Cañon Diablo Troilite (V-CDT)
308 standard.

309 *Oxygen isotopes in magmatic zircons*- Zircon $\delta^{18}\text{O}$ values were measured by SHRIMP on 3 samples of
310 quartz monzodiorite and quartz monzonite from the Falémé Batholith (RG10036, RG10039, RG10050)
311 and one sample of Bambadji Formation andesitic volcanoclastic rock (RG10030) (Fig. 2). Descriptions
312 of these rocks and the associated U-Pb zircon geochronology are provided by Allibone et al. (in press).
313 Oxygen ($^{18}\text{O}/^{16}\text{O}$) isotope ratios were measured for a selection of magmatic areas within zircon grains
314 in order to characterize the isotopic composition of the magma from which they crystallized and thereby

315 investigate the nature of the source(s) of these magmas. Following the U-Pb analyses, the SHRIMP U-
316 Pb pits, 1-2 μm deep, were lightly polished away and oxygen isotope analyses were made in exactly the
317 same location using SHRIMP II fitted with a Cs ion source and an electron gun for charge compensation
318 as described by Ickert et al. (2008). Oxygen isotope ratios were determined in multiple-collector mode
319 using an axial continuous electron multiplier (CEM) triplet collector, and two floating heads with
320 interchangeable CEM - Faraday Cups. The FC1 (Duluth Gabbro) reference zircons were analyzed to
321 monitor and correct for isotope fractionation. The measured $^{18}\text{O}/^{16}\text{O}$ ratios and calculated $\delta^{18}\text{O}$ values
322 have been normalized relative to a FC1 weighted mean $\delta^{18}\text{O}$ value of 5.61 ‰ (Fu et al., 2015).
323 Reproducibility in the FC1 reference zircon $\delta^{18}\text{O}$ value was ± 0.40 ‰ (2σ uncertainty) for the analytical
324 session. Temora 2 reference zircons were analysed in the same session as a secondary reference and
325 gave a $\delta^{18}\text{O}$ value of 8.04 ± 0.37 ‰, in agreement with that reported by Ickert et al. (2008).

326 **Results**

327 *Sulfur isotopes*

328 Sulfur isotope data are listed in full in Table 2. Auriferous sulfides from the Loulo Au deposits and their
329 satellites have $\delta^{34}\text{S}$ values between 5.8 and 15.5 ‰, with a mean of 9.6 ‰ ($n=74$) (Fig. 5a) (Fouillac et
330 al., 1993; Lambert-Smith et al., 2016b; Lawrence et al., 2013b). Diagenetic pyrite from the Kofi series
331 shows a broad range from 6.4 to 25.1 ‰. New $\delta^{34}\text{S}$ data (Fig. 5b) from Kabe West ranges from -4.6 to
332 3.4 ‰ ($n=9$; mean of -0.4 ‰). Sulfides at Baqata range from 5.5 to 11.8 ‰ ($n=4$; mean of 8.1 ‰).
333 Kolya exhibits $\delta^{34}\text{S}$ values from 4.2 to 14.2 ‰ ($n=5$; mean of 9 ‰). Mineralization at Boboti ranges
334 from 1.7 to 3.9 ‰ ($n=5$; mean of 2.5 ‰). Sulfides at the Karakaene Ndi skarn range from 2.8 to 11.9
335 ‰ ($n=11$; mean of 5.3 ‰) (Fig. 5c). Early sulfides disseminated within the massive Fe ore and hosted
336 in Fe oxide veins range from 2.8 to 4.4 ‰, whereas late sulfide-rich veins range from 4.9 to 11.9 ‰.

337 *Carbon isotopes*

338 Carbon isotope data are listed in full in Table 3. The $\delta^{13}\text{C}$ values for carbonate country rocks, and barren
339 and mineralized veins in the Loulo Mining District range from -21.7 to 3.8 ‰ (mean of -7.3 ‰; $n=79$).
340 The dataset for Au-bearing veins exhibits peaks in $\delta^{13}\text{C}$ at -10 ‰, -6 ‰ and at 0 ‰ (Fig. 6a). Data from
341 Kofi Series dolostones provide a local $\delta^{13}\text{C}$ values for carbonate country rocks. These range from -3.1
342 to 1.3 ‰ (mean of -0.5 ‰; $n=10$).

343 Sulfidized carbonate-bearing veins in the Kofi Series show a broad range in $\delta^{13}\text{C}$ values from -21.7 to
344 -3.7 ‰ ($n=55$) (Fig. 6a). This population is largely unimodal, with a minor negative skew toward lower
345 $\delta^{13}\text{C}$ values (mode at approximately -8 ‰). The Bambadji exploration targets (Fig. 6b) show a range in
346 $\delta^{13}\text{C}$ from -16.8 to -3.7 ‰ (mean of -8.4 ‰; $n=13$). Baqata veins range from -15.0 to -3.7 ‰ (mean of
347 -8.6 ‰; $n=6$). Kolya veins range from -8.8 to -5.1 ‰ (mean of -7.7 ‰; $n=5$). Kabe West ranges from -

348 8.6 to -5.9 ‰ (mean of -7.4 ‰; n=6). Gefa ranges from -16.8 to -7.0 ‰ (mean of -10.2 ‰; n=4). Gara,
349 Yalea, and Gounkoto show the greatest range of values, from -21.7 to -4.5 ‰ (mean of -11.6 ‰; n=32).
350 Gara shows a range from -14.4 to -4.5 ‰ (mean of -9.6 ‰; n=16), Yalea from -21.7 to -10.6 ‰ (mean
351 of -16.7 ‰; n=8), and Gounkoto from -13.6 to -6.3 ‰ (mean of -9.1 ‰; n=8). In contrast, barren (sulfide
352 absent) carbonate-bearing hydrothermal veins show a similar population distribution to carbonate
353 country rocks. This ranges from -2.4 to 3.8 ‰ (mean of -0.7 ‰; n=9) (Fig. 6a). Calcite from sulfide
354 veins at the Karakaene Ndi skarn deposit range from -4.1 to -1.8 ‰ (n=7; mean of -3.0 ‰) (Fig. 6c).

355 *Oxygen isotopes in carbonates*

356 Oxygen isotope data for carbonate minerals are listed in full in Table 3. The O isotope ratios of
357 carbonates in the Loulo district exhibit a wide range from 11.4 to 23.3 ‰ (n=79). The data are not
358 normally distributed and have a positive skew toward higher $\delta^{18}\text{O}$ values (Fig. 6d). Kofi series
359 limestones tend to exhibit heavier $\delta^{18}\text{O}$ values than hydrothermal veining, ranging between 19.1 and
360 23.3 ‰, with one outlying value at 15.1 ‰ (mean of 20.3 ‰; n=10). Barren hydrothermal veins are
361 indistinguishable from mineralized hydrothermal veins based on their O-isotopic composition (Fig. 6e).
362 Barren veins range from 11.7 to 21.1 ‰ (mean of 15.8 ‰; n=14). Mineralized veins range from 11.4
363 to 23.2 ‰ (mean of 15.6 ‰; n=55). Calcite from sulfide veins at the Karakaene Ndi skarn deposit range
364 from -12.0 to -13.5 ‰ (n=7; mean of -12.6 ‰) (Fig. 6f).

365 *Oxygen isotopes in magmatic zircons*

366 Oxygen isotope data in magmatic zircons is listed in full in Appendix Table A1. The zircon $\delta^{18}\text{O}$ values
367 obtained from Bambadji Formation andesitic volcanoclastic rock sample RG10030 range between 6.4
368 and 8.4 ± 0.5 ‰ with a weighted mean value of 7.2 ± 0.7 ‰ (MSWD of 13). However, a probability
369 density plot shows a minor mode at around 6.5 ‰, with scatter among higher values. All grains analysed
370 have U-Pb isotopic ratios < 10% discordant implying their oxygen isotope ratios are unlikely to have
371 been markedly affected by post crystallisation Pb-loss ref.

372 Zircons from two samples of the Highway Pluton (RG10036, RG10039) were analysed.. The 5 most
373 concordant zircon analyses in RG10036 have $\delta^{18}\text{O}$ ratios of between 7.0 and 8.4 ± 0.5 ‰. The two most
374 concordant analyses from RG10039 have associated $\delta^{18}\text{O}$ ratios of 7.0 and 8.1 ± 0.5 ‰, respectively.
375 Remaining discordant zircons from these two samples have $\delta^{18}\text{O}$ ratios (6.5 to 8.4 ‰), which are in
376 broad agreement with the range of values in concordant zircons in all the samples (6.4 to 8.4 ‰) and
377 may therefore be considered with the other data. The weighted mean for RG10036 is 7.9 ± 0.4 ‰
378 (MSWD of 8.4). RG10039 has too few analyses to be significant, though the weighted mean of 7.7 ‰
379 is in broad agreement with data from the other samples. A sample from the Balangouma Pluton, west
380 of Gara (RG10050), contains relatively abundant concordant zircon whose $\delta^{18}\text{O}$ ratios range between
381 6.5 and 8.1 ± 0.5 ‰ with a mean of 7.6 ± 0.3 ‰ (MSWD of 3.8).

382 A weighted mean of all the zircon data yields a $\delta^{18}\text{O}$ value of 7.6 ± 0.2 with an MSWD of 8.2. However,
383 a probability density plot of the entire dataset suggests that there are two general values recorded,
384 with a major mode at : a more prominent value around 7.9 ± 0.1 ‰ and a less prominent lower
385 value minor mode around 6.7 ± 0.2 ‰.

386 Discussion

387 *S-isotope Compositions and Sulfur Sources*

388 New $\delta^{34}\text{S}$ data from the Au occurrences at Kabe West, Baqata, Boboti, and Kolya (-4.6 to 14.2 ‰)
389 partially overlap the range of values for the Loulo Au deposits (5.8 to 15.5 ‰) and those of diagenetic
390 pyrite from the Kofi series (6.4 to 25.1 ‰), though they also extend to lower ratios (Fig. 5 a and b).
391 Lambert-Smith et al. (2016b) interpret these data to indicate that sulfur in the main Loulo Au deposits
392 is derived from a metasedimentary source. Sulfides at the Karakaene Ndi Fe skarn change from lower
393 isotopic values in early disseminated sulfides (2.8 to 4.4 ‰), to higher values in late sulfide-rich veins
394 (4.9 to 11.9 ‰), which overlap with the range of $\delta^{34}\text{S}$ in Kofi series diagenetic pyrite (Fig. 5c). This
395 suggests that paragenetically early sulfur in the skarn was dominantly sourced from magmatic fluids
396 ($\delta^{34}\text{S} = 0 \pm 2$ ‰) (Ohmoto, 1972), but as the hydrothermal system developed, sulfur with high $\delta^{34}\text{S}$ (> 4
397 ‰) was incorporated from the Kofi series metasedimentary rocks or the Bambadji Formation volcanic
398 rocks. Persistently low $\delta^{34}\text{S}$ values at the Boboti and Kabe West Au prospects (-4.6 to 3.9 ‰) imply a
399 magmatic sulfur source.

400 *C-isotope Compositions and Carbon Sources*

401 Carbonate minerals from barren hydrothermal veins and dolostone country rocks throughout the
402 southern Kofi Series have $\delta^{13}\text{C}$ values between -3.1 ‰ and 3.8 ‰ (Fig. 6a, b), with means of -0.7 and
403 -0.5 ‰, respectively. These values are typical for Paleoproterozoic marine carbonate (Strauss and
404 Moore, 1992). This indicates that barren veins likely formed through dissolution of carbonate minerals
405 in the host sedimentary rocks (Dietrich et al., 1983; Elmer et al., 2006; Lawrence et al., 2013b).
406 Compositions of auriferous veins in the Kofi Series are more heterogeneous, ranging from -21.7 to -3.7
407 ‰ (mean of -9.9 ‰) (Fig. 6a, b). The lowest ratios at Yalea (-19.5 to -21.7 ‰) (Lawrence et al., 2013b),
408 are within the $\delta^{13}\text{C}$ range of Precambrian organic matter, at -24.7 ± 6 ‰ (Schidlowski et al., 1975,
409 Papineau et al., 2010). This is similar to carbonaceous material in of the Paleoproterozoic Kumasi Basin
410 in Ghana, which yield mean $\delta^{13}\text{C}_{\text{org}}$ of -23 ± 5 ‰ (Mumin et al., 1996; Oberthuer et al., 1996). The $\delta^{13}\text{C}$
411 of auriferous veins from elsewhere in the Loulo district, including most data from Baqata, Kolya, Kabe
412 West and Gefa (Fig. 6b), fall between -16 and -4 ‰. These higher values could reflect contributions of
413 carbon from either (1) the Kofi Series dolostones or (2) magmatic CO_2 ($\delta^{13}\text{C}_{\text{CO}_2} \approx -5$ to -10 ‰; Ohmoto,
414 1972).

415 In either case, the range of compositions indicate a contribution of ^{13}C -depleted organic carbon to the
416 hydrothermal system (Fig. 6a). The two most probable mechanisms by which this might occur are: 1)
417 oxidation of graphite derived from organic matter ($\text{C} + \text{O}_2 \rightarrow \text{CO}_2$), or 2) hydrolysis of graphite ($2\text{C} +$
418 $2\text{H}_2\text{O} \rightarrow \text{CO}_2 + \text{CH}_4$). Application of isotopic fractionation factors (using the equations of Ohmoto and
419 Rye, 1979; Golyshev, et al. 1981; Horita, 2001) for average ore forming temperatures in the Loulo
420 district (ca. 320 °C; Lawrence et al., 2013b; Lambert-Smith et al., 2016b) suggests that *in situ* hydrolysis
421 of graphite in Kofi dolostones would produce CO_2 with $\delta^{13}\text{C} \geq -17.5$ ‰. Carbonate minerals precipitated
422 from this fluid between 295 and 340 °C (after Lawrence et al 2013b) would have $\delta^{13}\text{C}$ between of -18.1
423 and -19.2 ‰. This cannot therefore explain the lowest $\delta^{13}\text{C}$ values at Yalea. Alternatively, C-isotope
424 fractionation during hydrolysis could occur in the fluid source region. A fluid with $X(\text{CO}_2) = 0.2\text{-}0.3$
425 may be produced at temperatures of 500 to 520 °C at the greenschist-amphibolite transition (Elmer et
426 al., 2006). This could produce $\delta^{13}\text{C}_{\text{CO}_2}$ values as low as -20.8 ‰ yielding $\delta^{13}\text{C}_{\text{dolomite}}$ as low as -21.7 ‰,
427 depending on the initial $\delta^{13}\text{C}_{\text{org}}$ of the source material. In both cases we assume open system behaviour,
428 whereby CO_2 has undergone significant fractionation from the source graphite composition. This ^{13}C -
429 depleted fluid may then have interacted with country rocks in the Kofi Series or a fluid (brine?) of
430 differing composition, to produce the wide range of observed values.

431 The isotopic compositions of late carbonate-sulfide veining at the Karakaene Ndi Fe skarn deposit (-
432 4.1 to -1.8 ‰) are ~ 1 ‰ above the expected range of values for a magmatic fluid (Fig. 6c). A cooling
433 magmatic fluid should precipitate carbonate minerals with lower $\delta^{13}\text{C}$; therefore, it seems likely that
434 fluid mixing or wall rock interaction have modified the fluid. The most likely scenario is incorporation
435 of heavier $\delta^{13}\text{C}$ from the Kofi dolostones during hydrothermal activity around the skarn (Fig. 6a, c).
436 This is consistent with the interpretation of the $\delta^{34}\text{S}$ data (Fig. 5a, c).

437 *O-isotope Compositions and Oxygen Sources*

438 The $\delta^{18}\text{O}$ values in hydrothermal carbonate veins in the Kofi Series are more homogeneous compared
439 with the $\delta^{13}\text{C}$ values. Barren, sulfidized and auriferous veins have near identical mean $\delta^{18}\text{O}$ values of
440 15.8, 15.0, and 15.6 ‰, respectively, and range from 11.4 to 23.2 ‰ (Fig. 6 d, e, f). Isotopic
441 compositions above ~ 18 ‰ in auriferous veins are interpreted to represent disequilibrium as $\delta^{18}\text{O}$ in
442 paired quartz-dolomite samples at Goukoto and Yalea display $\delta^{18}\text{O}_{\text{quartz}} < \delta^{18}\text{O}_{\text{dolomite}}$ (Lambert-Smith
443 et al., 2016b; Lawrence et al., 2013b). This scenario suggests later modification of $\delta^{18}\text{O}_{\text{dolomite}}$ (Jenkin
444 et al., 1991). Most samples with $\delta^{18}\text{O}$ below ~ 14 ‰ are from the western Kofi Au prospects (Fig. 6d
445 and e), which show relatively high $\delta^{13}\text{C}$ values > -10 ‰ (Fig. 6b).

446 O-isotope compositions for Falémé batholith magmatic rocks are constrained by $\delta^{18}\text{O}_{\text{zircon}}$ data obtained
447 via SHRIMP analysis, the dominant population of which yield a $\delta^{18}\text{O}_{\text{zircon}}$ value of 7.9 ± 0.1 ‰ (2 SD;
448 $n=28$) (see App. Table A1). We estimated $\delta^{18}\text{O}_{\text{magma}}$ using melt-zircon fractionation values of Trail et

449 al. (2009) ($\Delta_{\text{melt-zircon}}$ at 800 °C = 1.7 ‰). We then applied the plagioclase-water fractionation values of
 450 Zheng (1993) ($\Delta_{\text{albite-H}_2\text{O}}$ at 700 °C = 0.2 ‰), to calculate a $\delta^{18}\text{O}_{\text{H}_2\text{O}}$ value of 9.4 ‰ for the Falémé
 451 batholith. Zircon crystallisation temperatures were estimated using data in Samperton et al. (2017). The
 452 maximum range of $\delta^{18}\text{O}_{\text{H}_2\text{O}}$ values for a magmatic-hydrothermal fluid exsolved from the Falémé
 453 batholith is 7.9 to 10.0 ‰. The average $\delta^{18}\text{O}_{\text{fluid}}$ value calculated from carbonates in the Loulo district
 454 overlaps this range at 10.2 ± 2.3 ‰ (calculated at 320 °C using the equations of Zheng, 1999). However,
 455 these data alone cannot constrain the fluid source as $\delta^{18}\text{O}_{\text{fluid}}$ values for local magmatic and metamorphic
 456 water (~4 to 25 ‰) overlap (Sheppard, 1986). At best these data are permissive of either, or both, fluid
 457 sources, and so must be interpreted in their geological context, together with $\delta^{13}\text{C}$ data. The western
 458 Kofi Au prospects have lower average $\delta^{18}\text{O}_{\text{fluid}}$ values of 9.1 ‰ (Baqata), 8.6 ‰ (Kolya), 8.3 ‰ (Kabe
 459 West), and 8.5 ‰ (Gefa), whereas the intrusive-hosted Boboti target has a significantly lower value of
 460 6.6 ‰. These lower values suggest the involvement of fluids sourced from the Falémé batholith in Au
 461 mineralization at these locations. Similarly, $\delta^{18}\text{O}_{\text{calcite}}$ at Karakaene Ndi, at temperatures of 550 °C, yield
 462 a $\delta^{18}\text{O}_{\text{fluid}}$ range from 9.6 to 11.1 ‰, overlapping the upper end of local magmatic water values.

463 *Carbon-Oxygen Isotope Modelling*

464 To test whether magmatic fluids may have contributed to the Au-bearing hydrothermal system of the
 465 Loulo district, we calculated the C-O isotope compositions of mixtures between a dilute metamorphic
 466 aqueous-carbonic fluid, and 1) a hypersaline brine derived from metaevaporites, and 2) a magmatic
 467 hydrothermal fluid sourced from the Falémé batholith. The equations of Schwinn et al. (2006) were
 468 used to calculate $\delta^{13}\text{C}$ values for carbonates precipitated from a mixed fluid ($\delta^{13}\text{C}_M$):

$$469 \quad \delta^{13}\text{C}_M = \left(\frac{m_B^* f_B}{m_B^* f_B + m_{AC}^* (1 - f_B)} \right) \cdot \delta^{13}\text{C}_B + \left(\frac{m_{AC}^* (1 - f_B)}{m_B^* f_B + m_{AC}^* (1 - f_B)} \right) \cdot \delta^{13}\text{C}_{AC}$$

470 Where $\delta^{13}\text{C}_B$, $\delta^{13}\text{C}_{AC}$, and represent C-isotope compositions for the brine, the aqueous-carbonic fluid,
 471 respectively. The molalities of carbon in the brine m_B^* and aqueous-carbonic fluid m_{AC}^* , have been
 472 calculated using the following equation:

$$473 \quad m_B^* = \frac{m_B}{(n_W + \sum m_{i,B})}$$

474 where n_w is the total number of moles H_2O in 1 kg water, m_B is the uncorrected molality of carbon in
 475 the brine, and $\sum m_{i,B}$ is the sum of the molalities of all solutes in the brine. This approach considers the
 476 significant salinity differences between the two fluids by correcting for total solute concentrations
 477 (Schwinn et al., 2006). These equations were adapted to model $\delta^{18}\text{O}_{\text{fluid}}$.

478 End member fluid isotopic and chemical compositions are detailed in Table 4. The starting isotopic
 479 composition for the brine ($\delta^{13}\text{C}_{\text{fluid}} = 1.8$ ‰ and $\delta^{18}\text{O}_{\text{fluid}} = 17.3$ ‰) is based on devolatilization of a

480 dolostone with similar initial $\delta^{13}\text{C}$ and $\delta^{18}\text{O}$ to that of Kofi Series dolostones (Valley, 1986). Starting
 481 compositions of the magmatic fluid ($\delta^{13}\text{C}_{\text{fluid}} = -6.0 \text{ ‰}$ and $\delta^{18}\text{O}_{\text{fluid}} = 9.4 \text{ ‰}$) are based upon $\delta^{18}\text{O}_{\text{H}_2\text{O}}$
 482 from the Falémé batholith (App. Table A1) and the accepted range of magmatic $\delta^{13}\text{C}_{\text{CO}_2}$ (Taylor, 1974).
 483 The aqueous-carbonic fluid is assumed to have the composition $\delta^{13}\text{C}_{\text{fluid}} = -27.0 \text{ ‰}$ and $\delta^{18}\text{O}_{\text{fluid}} = 10.2$
 484 ‰ . This represents a fluid derived from metamorphic devolatilization of C_{org} bearing sediments. $\delta^{13}\text{C}$
 485 and $\delta^{18}\text{O}$ of dolomite were calculated at ore forming temperatures of 320 °C.

486 Figure 7 shows that the isotopic character of auriferous hydrothermal veins at Loulo cannot be explained
 487 by binary mixing between end members of metamorphic aqueous-carbonic fluid and either a meta-
 488 evaporite derived brine, or a magmatic fluid from the Falémé batholith. We note above that the isotopic
 489 signature of the unequivocally magmatic Karakaene Ndi skarn does not correspond directly to Falémé
 490 magmatic fluid values. This suggests that any magmatic-hydrothermal fluid in even the most proximal
 491 parts of the hydrothermal system may be somewhat cryptic. We have therefore modelled the effects of
 492 water-rock reaction on the C-O isotope system (Fig. 7), with the objectives of (1) explaining the $\delta^{13}\text{C}$
 493 and $\delta^{18}\text{O}$ signature of the Karakaene Ndi skarn and (2) investigating the magmatic contributions to the
 494 Loulo Au deposits, particularly the prospects in the western Kofi Series. This was accomplished using
 495 the following equation, assuming open system behaviour (modified after Shelton, 1983):

$$496 \quad \delta_r^f = (\delta_r^i - \delta_w^i + \Delta) e^{\frac{-Wc_w}{Rc_r}} + \delta_w^i - \Delta$$

497 Where $_r$ and $_w$ denote rock and water (or mineral and fluid), respectively. δ^i and δ^f denote the initial
 498 and final isotopic composition, respectively. Δ is the fluid-mineral per mil fractionation as a function of
 499 temperature (in this case 320 °C for the metamorphic fluid and 550 °C for the magmatic-hydrothermal
 500 fluid). C indicates concentration, R mass of rock, and W mass of water. The reaction curves were
 501 modelled for water-rock ratios between 100 and 0.01. The metamorphic fluid was modelled at XCO_2
 502 = 0.2, and the magmatic-hydrothermal fluid at 0.11 (Lambert-Smith et al., 2016b, Lawrence et al.,
 503 2013b). End member fluid isotopic and chemical compositions are as detailed above (Table 4). Average
 504 Kofi dolostone compositions were used for the host rock.

505 *Interactions between the Loulo and Falémé Mineral Systems*

506 Carbonate veins from Karakaene Ndi fall along water-rock reaction pathways typical of magmatic-
 507 hydrothermal systems (Fig. 7) (e.g. Pass et al., 2014). These data represent a hot (~550 °C) magmatic
 508 fluid from the Falémé Batholith interacting with significantly cooler carbonate-rich wall rocks with high
 509 $\delta^{13}\text{C}$. This pattern is replicated in $\delta^{34}\text{S}$ data (Fig. 5c), where a shift to higher $\delta^{34}\text{S}$ in later veins suggests
 510 an influx of wall rock sulfur as the hydrothermal system began to cool and retrograde skarn
 511 mineralization began.

512 C-O isotope modelling indicates that water-rock reaction between a metamorphic fluid and carbonate-
513 rich Kofi Series host rocks was an important process at Gara, Yalea and Goukoto and can partly
514 explain the C and O isotopic compositions of these deposits (Fig. 7). Critically, the three world class
515 deposits at Loulo show limited isotopic evidence for direct contribution of magmatic volatiles, with the
516 possible exception of Gara (Fig. 7). In contrast, the Au prospects in the western Kofi Series at Baqata,
517 Kolya, Kabe West and Gefa (as well as limited data points from Gara) have higher $\delta^{13}\text{C}$ and lower $\delta^{18}\text{O}$
518 values than the main Loulo deposits, which fall between the aqueous carbonic fluid-dolostone and
519 magmatic brine-dolostone reaction curves (Fig. 7).

520 On the basis of these data, we suggest that mineralization in the small Au prospects adjacent to the
521 margin of the Falémé Batholith was deposited from a mixed aqueous-carbonic and magmatic fluid, both
522 of which had been modified through reaction with Kofi Series dolostone and/or Bambadji Formation
523 volcanic rocks prior to mixing. While isotopic values for the Kolya, Baqata and Gefa prospects are
524 largely in agreement with those of the main Loulo Au deposits, including their low $\delta^{34}\text{S}$ values (Fig. 5a,
525 b), those for Kabe West and Boboti plot at lower $\delta^{18}\text{O}$, implying a stronger magmatic-hydrothermal
526 affinity (Fig. 6b and 7). Kabe West and Boboti are both hosted within intensely albitized igneous rocks
527 on the margin of the Falémé batholith, which is intruded by multiple generations of small-scale dikes
528 and stocks consistent with an elevated contribution of magmatic volatiles. Furthermore, low $\delta^{18}\text{O}$ values
529 at Baqata, Kolya, and Gefa are consistent with the presence of thin diorite dikes within 5 m of
530 mineralization (Lambert-Smith, 2014a). These dikes may have exsolved small aliquots of magmatic-
531 hydrothermal fluid similar to those responsible for skarn alteration, resulting in the heterogeneous
532 isotopic signature of Au prospects in the western Kofi Series. It should also be noted that some of the
533 isotopic values for hydrothermal minerals in the western Kofi Au prospects could be generated simply
534 from a cooling end-member magmatic fluid.

535 *Metallogenic Model for the Loulo District*

536 Lambert-Smith et al. (2016c) reported that pre-ore hydrothermal tourmalines at Gara and Yalea North
537 were deposited from an ^{11}B -rich fluid whose isotopic character was comparable with metaevaporite
538 source rocks. While evaporite beds have not been identified in the Kofi series, the B-isotope data
539 suggest the marly dolostones in the west of the Kofi basin may have contained evaporitic horizons (Fig.
540 8a). The Falémé batholith intruded these marly dolostones and evaporite horizons (Fig. 2) between 2084
541 ± 8 Ma and 2070 ± 5 Ma, during which time the Falémé skarns also formed (Fig. 8 b and c). Field
542 relationships between albitization and magmatic rocks in the Kofi Series suggest NaCl, CO_2 and B were
543 initially mobilized during syn- D_1 metamorphism of Kofi Series dolostones, before Falémé magmatism,
544 giving rise to a paragenetically early brine and widespread associated albitic and tourmaline alteration.
545 Falémé magmatism now seems likely to have contributed both heat and magmatic-hydrothermal fluid
546 to this evolving system, synchronous with on-going D_2 metamorphism and minor transcurrent

547 deformation. These magmatic fluids may have evolved into high temperature saline brines through
548 reaction with the dolostones or mixing with a metamorphic brine derived from earlier devolatilization
549 of the dolostones and interbedded evaporites. This scenario would explain both the high fluid
550 temperatures (>400 °C) documented by Lawrence et al. (2013b) and the meta-evaporite B-isotope
551 signature described by Lambert-Smith et al. (2016c), as it seems likely that the dominant B reservoir in
552 such a scenario would be the evaporative wall rocks.. High thermal gradients and permissive structural
553 architecture allowed widespread circulation of this hybrid magmatic-hydrothermal and meta-evaporitic
554 brine, resulting in on-going, multi-phase, district-scale Na and B metasomatism prior to and during Au
555 mineralization (Lawrence et al., 2013b; Lambert-Smith et al., 2016a; Lambert-Smith et al., 2016b;
556 Lambert-Smith et al., 2016c) (Fig. 8b). At the Karakaene Ndi skarn high $\delta^{34}\text{S}$ and $\delta^{13}\text{C}$ values suggest
557 a contribution to the hydrothermal system from wall rocks with isotopic characteristics similar to the
558 Kofi dolostones. Similarly, at Gara a shift from high $\delta^{11}\text{B}$ (~12.7 ‰) to lower values (~5 ‰) indicates
559 that in places, brines containing both evaporite and magmatic components (hybrid) mixed with more
560 dilute aqueous-carbonic fluids during Au mineralization (Lambert-Smith et al., 2016c). This implies
561 that the hybrid brine contributed to the formation of both the Falémé skarns and the Loulo Au deposits.

562 Given that the aqueous-carbonic fluid is present in all Au deposits in the Loulo region, whereas the
563 hypersaline brine is absent at Yalea, it seems likely that the former was more important in terms of
564 introducing Au to the system. Stable isotope data from Au-related pyrite and arsenopyrite ($\delta^{34}\text{S}$ 5.8 to
565 9.6 ‰), quartz ($\delta^{18}\text{O}$ 15.8 to 16.3 ‰ yielding a mean $\delta^{18}\text{O}_{\text{fluid}}$ of approx. 9.7 ‰ at 320 °C), dolomite
566 ($\delta^{13}\text{C}$ -15.8 to -21.7 ‰) (Lawrence et al., 2013b) and tourmaline ($\delta^{11}\text{B}$ -0.5 to 9.3 ‰) (Lambert-Smith
567 et al., 2016c) at Yalea are all compatible with the aqueous-carbonic fluid being sourced from Kofi Series
568 siliciclastic metasedimentary and carbonate rocks (Rye and Ohmoto, 1974; Sheppard, 1986; van
569 Hinsberg et al., 2011) with a significant organic C component (Schidlowski et al., 1975). Our new data
570 and modelling show that the brine with which the aqueous-carbonic fluid mixed is likely to have
571 evolved from interaction between magmatic-hydrothermal fluid(s) and the Kofi Series dolostones (\pm
572 meta-evaporites). Heat from the intrusion of the Falémé Batholith could conceivably have perturbed the
573 local geothermal gradient sufficiently to drive this district scale hydrothermal system.

574 *Implications for Orogenic Au and other Hydrothermal Systems*

575 Our data suggest that magmatic fluids can make a significant contribution to some orogenic Au
576 mineralization. In the Loulo example magmatism, combined with highly reactive dolostone and
577 evaporitic country rocks resulted in generation of a hybrid brine that appears to have acted as a chemical
578 trap for this and other aqueous carbonic Au-bearing fluids.

579 Comparisons between the Loulo District and some iron oxide Cu-Au (IOCG) provinces are also
580 instructive. Deposits of the Carajás Mineral Province of northern Brazil are somewhat analogous in that
581 they feature hypersaline brines (up to 58 wt. % equiv. NaCl) (da Costa Silva et al., 2015), which have

582 derived their salt content from meta-evaporitic rocks (Xavier et al., 2008; Riehl and Cabral, 2018).
583 Intrusion of magma into evaporite bearing rocks has set up district-scale hydrothermal systems resulting
584 in abundant sodic and calcic alteration. Schwartz and Melcher (2004) and Lawrence et al. (2013a) have
585 both suggested that the Falémé skarns share characteristics with IOCG deposits. Notably, the skarns are
586 rich in low-Ti iron oxides and are associated with widespread and paragenetically early alteration
587 associated with both CO₂-rich and saline fluids. The Falémé skarns however, differ in that they contain
588 no economic Cu, only relatively low-grade Au, and are more intimately associated with magmatic rocks
589 than is typical for IOCG deposits (c.f. Williams et al., 2005).

590 The isotopic data largely supports a metamorphic devolatilization model for the system at Loulo (e.g.
591 Groves et al., 2019). Though the term may not be wholly appropriate in describing the Loulo deposits,
592 there is a clear metamorphic signature in the isotope data with deposits such as Yalea formed largely
593 without the influence of the hybrid magmatic-hydrothermal/evaporite-derived brine.

594

Conclusions

595 Taken together, our data suggest a critical role for magmatism in the development of early alteration
596 assemblages in the Loulo District, in the genesis of the Falémé iron skarns, and in those Au deposits
597 that formed in response to fluid mixing. In these deposits, including Gara and the minor Au occurrences
598 in close spatial association with dikes and sills on the margin of the Falémé Batholith, there is strong
599 indications that evolved magmatic fluids were present during mineralization.

600 We envisage a scenario where the Falémé Batholith intrudes the marly evaporite-bearing carbonate
601 rocks of the western Kofi Series. Fluids exsolved from the Falémé Batholith interacted with the marly
602 dolostones generating a hypersaline brine which circulated through the Kofi and Falémé lithologies.
603 This resulted in the widespread albitization and tourmalinization characteristic of the region, which
604 hardens certain lithologies providing a favourable competency contrast for Au-bearing fluids to exploit.
605 Early metasomatism is overprinted by orogenic-style Au and Fe skarn mineralization; the former related
606 to the incursion of aqueous-carbonic fluids. These fluids largely precipitate minerals due to pressure
607 fluctuations or water-rock reactions (Lambert-Smith et al., 2016b, Lawrence et al., 2013b), but in places
608 partially mix with the magmatic-evaporitic brines which provide a chemical trap for Au mineralization.
609 In this way, the intrusion of the Falémé Batholith played a direct role in the development of the Loulo
610 Au mineral system. Skarn formation is likely to have been promoted by the presence of Cl-rich brines,
611 which would have encouraged metal transport in FeCl₂ complexes.

612 Acknowledgements

613 This research was funded by Randgold Resources and Kingston University. Isotopic analyses were
614 carried out through a NERC Facilities Grant (IP-1252-0511). A. J. Boyce is funded by NERC support

615 to the Isotope Community Support Facility at SUERC. The authors wish to thank the technical staff at
616 SUERC and Kingston for their assistance in carrying out sample preparation and analysis. SHRIMP
617 zircon oxygen isotope data was acquired by Mark Fanning using the facilities at the Australian National
618 University as part of a collaborative program funded by Randgold Resources Ltd during 2014-2015.
619 We also wish to thank Larry Meinert and two anonymous reviewers for their constructive reviews,
620 which undoubtedly improved the manuscript.

621 **References**

- 622 Allibone, A., Teasdale, J., Cameron, G., Etheridge, M., Uttley, P., Soboh, A., Appiah-Kubi, J., Adanu, A.,
623 Arthur, R. and Mamphey, J., 2002, Timing and structural controls on gold mineralization at
624 the Bogoso gold mine, Ghana, West Africa: *Economic Geology*, v. 97, p. 949-969.
- 625 Allibone, A., Lawrence, D., Scott, J., Fanning, M., Lambert-Smith, J., Harbidge, R., Vargas, C., Turnbull,
626 R., Joel Holliday, J., Paleoproterozoic gold deposits of the Loulo district, western Mali:
627 Society of Economic Geologists Special Publication 23, 2020, in press.
- 628 Baratoux, L., Metelka, V., Naba, S., Jessell, M. W., Grégoire, M. and Ganne, J., 2011, Juvenile
629 Paleoproterozoic crust evolution during the Eburnean orogeny (~ 2.2–2.0 Ga), western
630 Burkina Faso: *Precambrian Research*, v. 191, p. 18-45.
- 631 Block, S., Ganne, J., Baratoux, L., Zeh, A., Parra-Avila, L., Jessell, M., Ailleres, L. and Siebenaller, L.,
632 2015, Petrological and geochronological constraints on lower crust exhumation during
633 Paleoproterozoic (Eburnean) orogeny, NW Ghana, West African Craton: *Journal of*
634 *Metamorphic Geology*, v. 33, p. 463-494.
- 635 Campbell Mccuaig, T. and Kerrich, R., 1998, P—T—t—deformation—fluid characteristics of lode gold
636 deposits: evidence from alteration systematics. *Ore Geology Reviews*, v. 12, p. 381-453.
- 637 Craig, H. 1957, Isotopic standards for carbon and oxygen and correction factors for mass-
638 spectrometric analysis of carbon dioxide: *Geochimica et cosmochimica acta*, v. 12, p. 133-
639 149.
- 640 Da Costa Silva, A. R., Villas, R. N. N., Lafon, J.-M., Craveiro, G. S. and Ferreira, V. P., 2015, Stable
641 isotope systematics and fluid inclusion studies in the Cu–Au Visconde deposit, Carajás
642 Mineral Province, Brazil: implications for fluid source generation: *Mineralium Deposita*, v.
643 50, p. 547-569.
- 644 Davis, D., Hirdes, W., Schaltegger, U. and Nunoo, E., 1994, U-Pb age constraints on deposition and
645 provenance of Birimian and gold-bearing Tarkwaian sediments in Ghana, West Africa:
646 *Precambrian Research*, v. 67, p. 89-107.
- 647 De Kock, G., Armstrong, R., Siegfried, H. and Thomas, E., 2011, Geochronology of the Birim
648 Supergroup of the West African craton in the Wa-Bolé region of west-central Ghana:
649 Implications for the stratigraphic framework: *Journal of African Earth Sciences*, v. 59, p. 1-40.
- 650 Dia, A., Van Schmus, W. and Kröner, A., 1997, Isotopic constraints on the age and formation of a
651 Palaeoproterozoic volcanic arc complex in the Kedougou Inlier, eastern Senegal, West Africa:
652 *Journal of African Earth Sciences*, v. 24, p. 197-213.
- 653 Dietrich, D., Mckenzie, J. A. and Song, H., 1983, Origin of calcite in syntectonic veins as determined
654 from carbon-isotope ratios: *Geology*, v. 11, p. 547-551.
- 655 Eglinger, A., Thébaud, N., Zeh, A., Davis, J., Miller, J., Parra-Avila, L. A., Loucks, R., Mccuaig, C. and
656 Belousova, E., 2017, New insights into the crustal growth of the Paleoproterozoic margin of
657 the Archean Kéména-Man domain, West African craton (Guinea): Implications for gold
658 mineral system: *Precambrian Research*, v. 292, p. 258-289.
- 659 Eichmann, R. and Schidlowski, M., 1975, Isotopic fractionation between coexisting organic carbon—
660 carbonate pairs in Precambrian sediments: *Geochimica et Cosmochimica Acta*, v. 39, p. 585-
661 595.

662 Elmer, F., White, R. and Powell, R., 2006, Devolatilization of metabasic rocks during greenschist–
663 amphibolite facies metamorphism: *Journal of Metamorphic Geology*, v. 24, p. 497-513.

664 Fontaine, A., Eglinger, A., Ada, K., André-Mayer, A.-S., Reisberg, L., Siebenaller, L., Le Mignot, E.,
665 Ganne, J. and Poujol, M., 2017, Geology of the world-class Kiaka polyphase gold deposit,
666 West African Craton, Burkina Faso: *Journal of African Earth Sciences*, v. 126, p. 96-122.

667 Fougereuse, D., Micklethwaite, S., Ulrich, S., Miller, J., Godel, B., Adams, D. T. and Mccuaig, T. C.,
668 2017, Evidence for two stages of mineralization in West Africa’s largest gold deposit: Obuasi,
669 Ghana: *Economic Geology*, v. 112, p. 3-22.

670 Fouillac, A., Dommaget, A. and Milési, J., 1993, A carbon, oxygen, hydrogen and sulfur isotopic
671 study of the gold mineralization at Loulo, Mali. *Chemical geology*, v. 106, p. 47-62.

672 Frimmel, H. E. and Hennigh, Q., 2015, First whiffs of atmospheric oxygen triggered onset of crustal
673 gold cycle: *Mineralium Deposita*, v. 50, p. 5-23.

674 Fu, B., Bröcker, M., Ireland, T.R., Holden, P., and Kinsley, L., 2015, Zircon U-Pb, O, and Hf isotopic
675 constraints on Mesozoic magmatism in the Cyclades, Aegean Sea, Greece: *Geologische
676 Rundschau*, v. 104, p. 75–87.

677 Gaboury, D., 2013, Does gold in orogenic deposits come from pyrite in deeply buried carbon-rich
678 sediments?: Insight from volatiles in fluid inclusions: *Geology*, v. 41, p. 1207-1210.

679 Ganne, J., De Andrade, V., Weinberg, R. F., Vidal, O., Dubacq, B., Kagambega, N., Naba, S., Baratoux,
680 L., Jessell, M. and Allibon, J., 2011, Modern-Style Plate Subduction Preserved In The
681 Palaeoproterozoic West African Craton: *Nature Geoscience*, v. 5, p. 60.

682 Goldfarb, R. J., André-Mayer, A.-S., Jowitt, S. M. and Mudd, G. M., 2017, West Africa: The world’s
683 premier Paleoproterozoic gold province: *Economic Geology*, v. 112, p. 123-143.

684 Goldfarb, R. J. and Groves, D. I., 2015, Orogenic gold: Common or evolving fluid and metal sources
685 through time: *Lithos*, v. 233, p. 2-26.

686 Goldfarb, R. J., Newberry, R. J., Pickthorn, W. J. and Gent, C. A., 1991, Oxygen, hydrogen, and sulfur
687 isotope studies in the Juneau gold belt, southeastern Alaska; constraints on the origin of
688 hydrothermal fluids: *Economic geology*, v. 86, p. 66-80.

689 Golyshev, S.I., Padalko, N.L. and Pechenkin, S.A., 1981, Fractionation of stable oxygen and carbon
690 isotopes in carbonate systems: *Geochemistry International* v. 18, p. 85-99.

691 Grenholm, M., Jessell, M. and Thébaud, N., 2019, A geodynamic model for the Paleoproterozoic (ca.
692 2.27–1.96 Ga) Birimian Orogen of the southern West African Craton—Insights into an
693 evolving accretionary-collisional orogenic system: *Earth-Science Reviews*, v. 192, p. 138-193

694 Groves, D. I., Goldfarb, R. J., Gebre-Mariam, M., Hagemann, S. and Robert, F., 1998, Orogenic gold
695 deposits: a proposed classification in the context of their crustal distribution and relationship
696 to other gold deposit types: *Ore geology reviews*, v. 13, p. 7-27.

697 Groves, D. I., Santosh, M., Deng, J., Wang, Q., Yang, L. and Zhang, L., 2019, A holistic model for the
698 origin of orogenic gold deposits and its implications for exploration: *Mineralium Deposita*,
699 pp. 1-18.

700 Gueye, M., Siegesmund, S., Wemmer, K., Pawlig, S., Drobe, M., Nolte, N. and Layer, P., 2007, New
701 evidences for an early Birimian evolution in the West African Craton: An example from the
702 Kedougou-Kenieba inlier, southeast Senegal: *South African Journal of Geology*, v. 110, p.
703 511-534.

704 Hein, K. A., 2010, Succession of structural events in the Goren greenstone belt (Burkina Faso):
705 implications for West African tectonics: *Journal of African Earth Sciences*, 56, p. 83-94.

706 Henley, R.W., Norris, R.J., and Paterson, C.J., 1976, Multistage ore genesis in the New Zealand
707 Geosyncline: a history of post-metamorphic lode emplacement: *Mineralium Deposita*, v. 11,
708 p. 180-196.

709 Hirdes, W. and Davis, D., 2002, U–Pb geochronology of paleoproterozoic rocks in the southern part
710 of the Kedougou-Kenieba Inlier, Senegal, West Africa: evidence for diachronous accretionary
711 development of the Eburnean province: *Precambrian Research*, v. 118, p. 83-99.

712 Horita, J., 2001. Carbon isotope exchange in the system CO₂-CH₄ at elevated temperatures:
713 *Geochimica et Cosmochimica Acta*, v. 65, p. 1907-1919.

714 Ickert, R.B., Hiess, J., Williams, I.S., Holden, P., Ireland, T.R., Lanc, P., Schram, N., Foster, J.J. and
715 Clement, S.W., 2008, Determining high precision, in situ, oxygen isotope ratios with a
716 SHRIMP II: Analyses of MPI-DING silicate-glass reference materials and zircon from
717 contrasting granites: *Chemical Geology* v. 257, p. 114-128.

718 Jenkin, G. R. T., Linklater, C. and Fallick, A. E., 1991, Modeling of mineral $\delta^{18}\text{O}$ values in an igneous
719 aureole: Closed-system model predicts apparent open-system $\delta^{18}\text{O}$ values: *Geology*, v. 19,
720 p. 1185-1188.

721 John, T., Klemd, R., Hirdes, W. and Loh, G., 1999, The metamorphic evolution of the
722 paleoproterozoic (Birimian) volcanic Ashanti belt (Ghana, West Africa): *Precambrian*
723 *Research*, 98, p. 11-30.

724 Kerrich, R. and Wyman, D., 1990, Geodynamic setting of mesothermal gold deposits: An association
725 with accretionary tectonic regimes: *Geology*, v. 18, p. 882-885.

726 Lambert-Smith, J. S., 2014, The geology, structure and metallogenesis of the world class Loulo-
727 Bambadji Au district in Mali and Senegal, West Africa: Unpublished Ph.D. thesis, Kingston
728 upon Thames, UK, Kingston University London, 354 p.

729 Lambert-Smith, J. S., Lawrence, D. M., Müller, W. and Treloar, P. J., 2016a, Palaeotectonic setting of
730 the south-eastern Kédougou-Kéniéba Inlier, West Africa: New insights from igneous trace
731 element geochemistry and U-Pb zircon ages: *Precambrian Research*, v. 274, p. 110-135.

732 Lambert-Smith, J. S., Lawrence, D. M., Vargas, C. A., Boyce, A. J., Treloar, P. J. and Herbert, S., 2016b,
733 The Gounkoto Au deposit, West Africa: Constraints on ore genesis and volatile sources from
734 petrological, fluid inclusion and stable isotope data: *Ore Geology Reviews*, v. 78, p. 606-622.

735 Lambert-Smith, J. S., Rocholl, A., Treloar, P. J. and Lawrence, D. M., 2016c, Discriminating fluid
736 source regions in orogenic gold deposits using B-isotopes: *Geochimica et Cosmochimica*
737 *Acta*, v. 194, p. 57-76.

738 Lawrence, D. M., Lambert-Smith, J. S. and Treloar, P. J., 2016, A Review of Gold Mineralization in
739 Mali, In Bouabdellah, M. and Slack, J. F. (eds.) *Mineral Deposits of North Africa*. Springer
740 International Publishing. pp. 327-352.

741 Lawrence, D. M., Treloar, P. J., Rankin, A. H., Harbidge, P. and Holliday, J., 2013a, The geology and
742 mineralogy of the Loulo mining district, Mali, West Africa: Evidence for two distinct styles of
743 orogenic gold mineralization: *Economic Geology*, v. 108, p. 199-227.

744 Lawrence, D. M., Treloar, P. J., Rankin, A. H., Boyce, A. and Harbidge, P., 2013b, A fluid inclusion and
745 stable isotope study at the Loulo mining district, Mali, West Africa: Implications for multfluid
746 sources in the generation of orogenic gold deposits: *Economic Geology*, v. 108, p. 229-257.

747 Lebrun, E., Thébaud, N., Miller, J., Ulrich, S., Bourget, J. and Terblanche, O., 2016, Geochronology
748 and lithostratigraphy of the Siguiri district: Implications for gold mineralisation in the Siguiri
749 Basin (Guinea, West Africa): *Precambrian Research*, v. 274, p. 136-160.

750 Loh, G., Hirdes, W., Anani, C., Davis, D. W. and Vetter, U. K., 2000, Explanatory Notes for the
751 Geological Map of-Southwest Ghana 1: 100,000-Sekondi (0402A) and Axim (0403B) Sheets.

752 Mcfarlane, H. B., Ailleres, L., Betts, P., Ganne, J., Baratoux, L., Jessell, M. W., and Block, S., 2019,
753 Episodic collisional orogenesis and lower crust exhumation during the Palaeoproterozoic
754 Eburnean Orogeny: Evidence from the Sefwi Greenstone Belt, West African Craton:
755 *Precambrian Research*, v. 325, p. 88-110.

756 Mann, J. L., Vocke Jr, R. D. and Kelly, W. R., 2009, Revised $\delta^{34}\text{S}$ reference values for IAEA sulfur
757 isotope reference materials S-2 and S-3: *Rapid Communications in Mass Spectrometry: An*
758 *International Journal Devoted to the Rapid Dissemination of Up-to-the-Minute Research in*
759 *Mass Spectrometry*, v. 23, p. 1116-1124.

760 Markwitz, V., Hein, K. A. A., Jessell, M. W. and Miller, J., 2016, Metallogenic portfolio of the West
761 Africa craton: *Ore Geology Reviews*, v. 78, p. 558-563.

762 Masurel, Q., Thébaud, N., Miller, J. and Ulrich, S., 2017a, The tectono-magmatic framework to gold
763 mineralisation in the Sadiola-Yatela gold camp and implications for the paleotectonic setting
764 of the Kédougou-Kéniéba inlier, West Africa: *Precambrian Research*, v. 292, p. 35-56.

765 Masurel, Q., Thébaud, N., Miller, J., Ulrich, S., Hein, K. A., Cameron, G., Béziat, D., Bruguier, O. and
766 Davis, J. A., 2017b, Sadiola Hill: A world-class carbonate-hosted gold deposit in Mali, West
767 Africa: *Economic Geology*, v. 112, p. 23-47.

768 Masurel, Q., Thébaud, N., Miller, J., Ulrich, S., Roberts, M. P. and Béziat, D., 2017c, The Alamoutala
769 Carbonate-Hosted Gold Deposit, Kédougou-Kéniéba Inlier, West Africa: *Economic Geology*, v.
770 112, p. 49-72.

771 Mcfarlane, C. R., Mavrogenes, J., Lentz, D., King, K., Allibone, A. and Holcombe, R., 2011, Geology
772 and intrusion-related affinity of the Morila gold mine, southeast Mali: *Economic Geology*, v.
773 106, p. 727-750.

774 Mumin, A., Fleet, M. and Longstaffe, F., 1996, Evolution of hydrothermal fluids in the Ashanti gold
775 belt, Ghana; stable isotope geochemistry of carbonates, graphite, and quartz: *Economic
776 Geology*, v. 91, p. 135-148.

777 Norris, R.J. and Henley, R.W., 1976, Dewatering of a metamorphic pile. *Geology*, v. 4, p. 333-336.

778 Oberthuer, T., Mumm, A. S., Vetter, U., Simon, K. and Amanor, J. A., 1996, Gold mineralization in the
779 Ashanti Belt of Ghana; genetic constraints of the stable isotope geochemistry: *Economic
780 Geology*, v. 91, p. 289-301.

781 Oberthür, T., Vetter, U., Davis, D. W. and Amanor, J. A., 1998, Age constraints on gold mineralization
782 and Paleoproterozoic crustal evolution in the Ashanti belt of southern Ghana: *Precambrian
783 Research*, v. 89, p. 129-143.

784 Ohmoto, H., 1972, Systematics of sulfur and carbon isotopes in hydrothermal ore deposits: *Economic
785 Geology*, v. 67, p. 551-578.

786 Ohmoto, H. and Rye, R.O., 1979, Isotopes of sulfur and carbon. In: Barnes, H.I. (Editor),
787 Geochemistry of hydrothermal ore deposits. 2nd Edition, John Wiley and Sons, New York,
788 pp. 509-567.

789 Papineau, D., De Gregorio, B. T., Cody, G. D., Fries, M. D., Mojzsis, S. J., Steele, A., Stroud, R. M. and
790 Fogel, M. L., 2010, Ancient graphite in the Eoarchean quartz–pyroxene rocks from Akilia in
791 southern West Greenland I: Petrographic and spectroscopic characterization: *Geochimica et
792 Cosmochimica Acta*, v. 74, p. 5862-5883.

793 Parra-Avila, L. A., Belousova, E., Fiorentini, M. L., Baratoux, L., Davis, J., Miller, J. and Mccuaig, T. C.,
794 2016, Crustal evolution of the Paleoproterozoic Birimian terranes of the Baoulé-Mossi
795 domain, southern West African Craton: U–Pb and Hf-isotope studies of detrital zircons:
796 *Precambrian Research*, v. 274, p. 25-60.

797 Parra-Avila, L. A., Belousova, E., Fiorentini, M. L., Eglinger, A., Block, S. and Miller, J., 2018, Zircon Hf
798 and O-isotope constraints on the evolution of the Paleoproterozoic Baoulé-Mossi domain of
799 the southern West African Craton: *Precambrian Research*, v. 306, p. 174-188.

800 Parra-Avila, L. A., Bourassa, Y., Miller, J., Perrouty, S., Fiorentini, M. L. and Campbell Mccuaig, T.,
801 2015, Age constraints of the Wassa and Benso mesothermal gold deposits, Ashanti Belt,
802 Ghana, West Africa: *Journal of African Earth Sciences*, v. 112, p. 524-535.

803 Pass, H. E., Cooke, D. R., Davidson, G., Maas, R., Dipple, G., Rees, C., Ferreira, L., Taylor, C. and Deyell,
804 C. L., 2014, Isotope geochemistry of the Northeast zone, Mount Polley alkalic Cu-Au-Ag
805 porphyry deposit, British Columbia: A case for carbonate assimilation: *Economic Geology*, v.
806 109, p. 859-890.

807 Perrouty, S., Aillères, L., Jessell, M. W., Baratoux, L., Bourassa, Y. and Crawford, B., 2012, Revised
808 Eburnean geodynamic evolution of the gold-rich southern Ashanti Belt, Ghana, with new
809 field and geophysical evidence of pre-Tarkwaian deformations: *Precambrian Research*, v.
810 204, p. 12-39.

811 Petersson, A., Scherstén, A. and Gerdes, A., 2018, Extensive reworking of Archaean crust within the
812 Birimian terrane in Ghana as revealed by combined zircon U-Pb and Lu-Hf isotopes:
813 *Geoscience Frontiers*, v. 9, p. 173-189.

814 Phillips, G. N. and Powell, R., 1993, Link between gold provinces: *Economic Geology*, v. 88, p. 1084-
815 1098.

816 Phillips, G. N. and Powell, R., 2010, Formation of gold deposits: a metamorphic devolatilization
817 model: *Journal of Metamorphic Geology*, v. 28, p. 689-718.

818 Pitcairn, I. K., Teagle, D. A., Craw, D., Olivo, G. R., Kerrich, R., and Brewer, T. S., 2006, Sources of
819 metals and fluids in orogenic gold deposits: insights from the Otago and Alpine Schists, New
820 Zealand: *Economic Geology*, v. 101, p. 1525-1546.

821 Pitcairn, I. K., Craw, D., and Teagle, D. A., 2014, The gold conveyor belt: Large-scale gold mobility in
822 an active orogen: *Ore Geology Reviews*, v. 62, p. 129-142.

823 Riehl, W. and Cabral, A.R., 2018, Meta-evaporite in the Carajás mineral province, northern Brazil:
824 *Mineralium Deposita*, v. 53, p. 895-902.

825 Robinson, B. W. and Kusakabe, M., 1975, Quantitative preparation of sulfur dioxide, for sulfur-
826 34/sulfur-32 analyses, from sulfides by combustion with cuprous oxide: *Analytical Chemistry*,
827 v. 47, p. 1179-1181.

828 Randgold Resources Ltd., 2017, Annual report. www.randgoldresources.com

829 Rosenbaum, J. and Sheppard, S. M. F. 1986, An isotopic study of siderites, dolomites and ankerites at
830 high temperatures: *Geochimica et Cosmochimica Acta*, v. 50, p. 1147-1150.

831 Rye, R. O. and Ohmoto, H., 1974, Sulfur and carbon isotopes and ore genesis: a review: *Economic*
832 *Geology*, v. 69, p. 826-842.

833 Samperton, K. M., Bell, E. A., Barboni, M., Keller, C. B. and Schoene, B., 2017, Zircon age-
834 temperature-compositional spectra in plutonic rocks: *Geology*, v. 45, p. 983-986.

835 Schidlowski, M., Eichmann, R. and Junge, C. E., 1975, Precambrian sedimentary carbonates: carbon
836 and oxygen isotope geochemistry and implications for the terrestrial oxygen budget:
837 *Precambrian Research*, v. 2, p. 1-69.

838 Schwartz, M. and Melcher, F., 2004, The Faleme Iron District, Senegal. *Economic Geology*, v. 99, p.
839 917-939.

840 Schwinn, G., Wagner, T., Baatartsogt, B. and Markl, G., 2006, Quantification of mixing processes in
841 ore-forming hydrothermal systems by combination of stable isotope and fluid inclusion
842 analyses: *Geochimica et Cosmochimica Acta*, v. 70, p. 965-982.

843 Sharp, Z., 2017, Principles of stable isotope geochemistry (digitalrepository.unm.edu).

844 Shelton, K. L., 1983, Composition and origin of ore-forming fluids in a carbonate-hosted porphyry
845 copper and skarn deposit; a fluid inclusion and stable isotope study of Mines Gaspé, Quebec:
846 *Economic Geology*, v. 78, p. 387-421.

847 Sheppard, S. M. F., 1986, Chapter 6. Characterization and Isotopic Variations in Natural Waters:
848 *Stable Isotopes in High Temperature Geological Processes*.

849 Spence-Jones, C. P., Jenkin, G. R. T., Boyce, A. J., Hill, N. J. and Sangster, C. J. S., 2018, Tellurium,
850 magmatic fluids and orogenic gold: An early magmatic fluid pulse at Cononish gold deposit,
851 Scotland: *Ore Geology Reviews*, v. 102, p. 894-905.

852 Strauss, H. and Moore, T., 1992, Abundances and isotopic compositions of carbon and sulfur species
853 in whole rock and kerogen samples: *The Proterozoic biosphere: A multidisciplinary study*, pp.
854 709-798.

855 Taylor, H., 1974, The application of oxygen and hydrogen isotope studies to problems of
856 hydrothermal alteration and ore deposition: *Economic geology*, v. 69, p. 843-883.

857 Taylor, P. N., Moorbath, S., Leube, A. and Hirdes, W., 1992, Early Proterozoic crustal evolution in the
858 Birimian of Ghana: constraints from geochronology and isotope geochemistry: *Precambrian*
859 *Research*, v. 56, p. 97-111.

- 860 Thébaud, N., Allibone, A., Masurel, Q., Eglinger, A., Davis, J., André-Mayer, A., Miller, J. And Jessell,
861 M, The Paleoproterozoic (Rhyacian) gold deposits of West Africa: *Society of Economic*
862 *Geologists Special Publication 23*, 2020, in press.
- 863 Tomkins, A. G., 2013, On the source of orogenic gold. *Geology*, v. 41, p. 1255-1256.
- 864 Trail, D., Bindeman, I. N., Watson, E. B. and Schmitt, A. K., 2009, Experimental calibration of oxygen
865 isotope fractionation between quartz and zircon: *Geochimica et Cosmochimica Acta*, v. 73, p.
866 7110-7126.
- 867 Treloar, P., Lawrence, D., Senghor, D., Boyce, A. and Harbidge, P., 2015, The Massawa gold deposit,
868 Eastern Senegal, West Africa: an orogenic gold deposit sourced from magmatically derived
869 fluids? *Geological Society, London, Special Publications*, v. 393, p. 135-160.
- 870 Tshibubudze, A., Hein, K. A. and Mccuaig, T. C., 2015, The relative and absolute chronology of strato-
871 tectonic events in the Gorom-Gorom granitoid terrane and Oudalan-Gorouol belt, northeast
872 Burkina Faso: *Journal of African Earth Sciences*, v. 112, p. 382-418.
- 873 Valley, J. W., 1986, Stable isotope geochemistry of metamorphic rocks: *Reviews in Mineralogy and*
874 *Geochemistry*, v. 16, p. 445-489.
- 875 Van Hinsberg, V. J., Henry, D. J. and Marschall, H. R., 2011, Tourmaline: an ideal indicator of its host
876 environment: *The Canadian Mineralogist*, v. 49, p. 1-16.
- 877 Vidal, M., Gumiaux, C., Cagnard, F., Pouclet, A., Ouattara, G. and Pichon, M., 2009, Evolution of a
878 Paleoproterozoic “weak type” orogeny in the West African Craton (Ivory Coast):
879 *Tectonophysics*, v. 477, p. 145-159.
- 880 White, A., Burgess, R., Charnley, N., Selby, D., Whitehouse, M., Robb, L. and Waters, D., 2014,
881 Constraints on the timing of late-Eburnean metamorphism, gold mineralisation and regional
882 exhumation at Damang mine, Ghana: *Precambrian Research*, v. 243, p. 18-38.
- 883 Williams, P. J., Barton, M. D., Johnson, D. A., Fontboté, L., De Haller, A., Mark, G., Oliver, N. H. and
884 Marschik, R., 2005, Iron oxide copper-gold deposits: Geology, space-time distribution, and
885 possible modes of origin: *Economic Geology*, pp. 371-405.
- 886 Wyman, D. A., Cassidy, K. F. and Hollings, P., 2016, Orogenic gold and the mineral systems approach:
887 Resolving fact, fiction and fantasy: *Ore Geology Reviews*, v. 78, 322-335.
- 888 Xavier, R. P., Wiedenbeck, M., Trumbull, R. B., Dreher, A. M., Monteiro, L. V., Rhede, D., De Araújo, C.
889 E. and Torresi, I., 2008, Tourmaline B-isotopes fingerprint marine evaporites as the source of
890 high-salinity ore fluids in iron oxide copper-gold deposits, Carajas Mineral Province (Brazil) :
891 *Geology*, v. 36, p. 743-746.
- 892 Xue, Y., Campbell, I., Ireland, T. R., Holden, P. and Armstrong, R., 2013, No mass-independent sulfur
893 isotope fractionation in auriferous fluids supports a magmatic origin for Archean gold
894 deposits: *Geology*, v. 41, p. 791-794.
- 895 Yardley, B. W. and Cleverley, J. S., 2015, The role of metamorphic fluids in the formation of ore
896 deposits: *Geological Society, London, Special Publications*, v. 393, p. 117-134.
- 897 Zheng, Y.-F., 1993, Calculation of oxygen isotope fractionation in hydroxyl-bearing silicates: *Earth*
898 *and Planetary Science Letters*, v. 120, p. 247-263.
- 899 Zheng, Y.-F., 1999, Oxygen isotope fractionation in carbonate and sulfate minerals: *Geochemical*
900 *Journal*, v. 33, p. 109-126.

901

902

903 **Table captions**

904 Table 1 – Summary of key characteristics of Au and Fe mineralization in the Loulo District.

905 Table 2 - Table summarising stable sulfur isotope data from the Loulo Mining District. * - denotes data
906 from Fouillac et al. (1993). † - denotes data from Lawrence et al. (2013b). ‡ - denotes data from
907 Lambert-Smith et al. (2016b).

908 Table 3 – Table summarising stable carbon and oxygen isotope data from the Loulo Mining District. *
909 - denotes data from Fouillac et al. (1993). † - denotes data from Lawrence et al. (2013b). ‡ - denotes
910 data from Lambert-Smith et al. (2016b).

911 Table 4 – Chemical and isotopic fluid compositions used for end member components in fluid mixing
912 and fluid-rock reaction models.

913 **Figure captions**

914 Fig. 1. Geological map of the southern West Africa Craton, highlighting the distribution of Au deposits
915 (Modified after Baratoux et al., 2011; Fontaine et al., 2017; Thebaud et al. In Press). Location of major
916 Au deposits are based on those reported in Markwitz et al. (2016), and Goldfarb et al. (2017).

917 Fig. 2. Geological map of the Loulo Mining District in the south eastern region of the Kédougou-
918 Kéniéba inlier, with studied Au occurrences highlighted. Modified after Lawrence et al. (2013a), and
919 Lambert-Smith et al. (2016c).

920 Fig. 3. Key alteration and ore mineral textures at Karakaene Ndi. (A) photograph of coarse epidote-
921 albite-calcite vein cross cutting albitized igneous rock with envelopes of dark green actinolite
922 replacement in the wall rock and Fe-rich halos encroaching on the albitized rock. Photomicrographs of
923 (B) albitized wall rock with relict phenocrysts (replaced by albite) (XPL); (C) fine fibrous actinolite
924 replacing wall rock with minor magnetite mineralization (PPL); (D) albitized wall rock overprinted by
925 Fe-rich carbonate and disseminated actinolite with minor pyrite (PPL) and; (E) coarse intergrown
926 epidote and albite in cross cutting vein (XPL). Photographs of ore textures in diamond drill core from
927 Karakaene Ndi showing: (F) massive magnetite replacement with weak disseminated pyrite overprint
928 and; (G) late calcite-pyrite-chlorite vein cross cutting magnetite mineralization.

929 Fig. 4. Field photographs showing (A) typical marly dolostones country rock with highly deformed
930 calcite veining, argillaceous layers and graphitic material. (B) Ankerite-quartz-pyrite stockwork ore
931 characteristic of the Gara and Goukoto deposit (highly subordinate in the latter), the P64 satellite, and
932 the Baqata and Kolya exploration targets. (C) Auriferous ankerite-quartz-pyrite veins cross cutting
933 phyllic wall rock alteration at the Yalea deposit. (D) An example of sulfide-bearing carbonate veins
934 with Au concentrations below the detection limit of fire assay in the meter of core sampled. (E) Barren

935 veining in unaltered and unmineralized Kofi Series metasedimentary country rock. (F) Folded, sulfide-
936 free veining in weakly altered, unmineralized metasedimentary host rock. (G) Sulfide-bearing veins
937 from the Kofi Series with fire assay results below detection limit (<0.01 ppm).

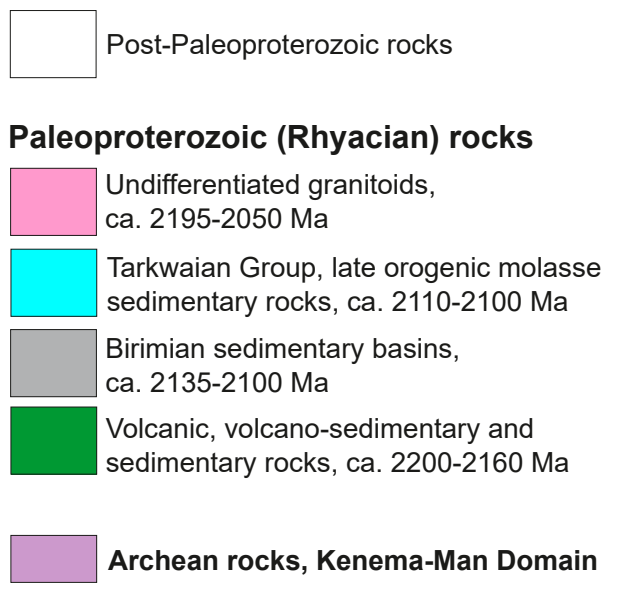
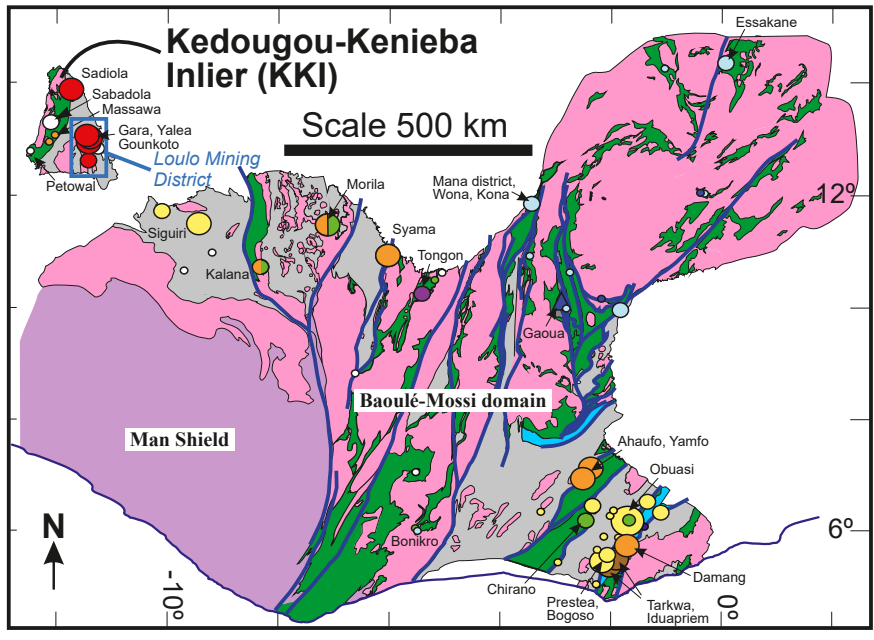
938 Fig. 5. Histograms showing $\delta^{34}\text{S}$ data from pyrite at (A) the Loulo Au deposits (Fouillac et al., 1993,
939 Lawrence et al., 2013b, Lambert-Smith et al., 2016b, Lambert-Smith, 2014b) and diagenetic pyrite from
940 the Kofi series dolostones, (B) the Kabe West, Kolya, Baqata and Bobotie exploration targets, (C) the
941 Karakaene Ndi skarn deposit, with paragenetic breakdown between sulfides disseminated in the iron ore
942 and those hosted in cross cutting veins (inset).

943 Fig. 6. Histograms showing $\delta^{13}\text{C}$ data from (A) ankerite and dolomite in auriferous hydrothermal veins,
944 barren hydrothermal veins, and carbonate country rocks from the Loulo-Goukoto complex, including
945 the Gara, Yalea and Goukoto mines (data from Fouillac et al., 1993, Lawrence et al., 2013b, Lambert-
946 Smith et al., 2016b); (B) ankerite and dolomite in auriferous and barren hydrothermal veins from the
947 Bambadji exploration targets, Gefa, Boboti, Kabe West, Kolya and Baqata; (C) calcite from late
948 hydrothermal veins at the Karakaene Ndi iron skarn deposit. Fields of typical C-isotope characteristics
949 of Precambrian marine carbonates and organic carbon are indicated (Schidlowski et al., 1975, Eichmann
950 and Schidlowski, 1975). Histograms showing $\delta^{18}\text{O}$ data from (D) ankerite and dolomite in auriferous
951 hydrothermal veins, barren hydrothermal veins, and carbonate country rocks from the Loulo-Goukoto
952 complex; (E) ankerite and dolomite in auriferous and barren hydrothermal veins from the Bambadji
953 exploration targets, Gefa, Boboti, Kabe West, Kolya and Baqata; (F) calcite from late hydrothermal
954 veins at the Karakaene Ndi iron skarn deposit. Number of samples and key is equivalent to (A), (B) and
955 (C).

956 Fig. 7. $\delta^{18}\text{O}$ versus $\delta^{13}\text{C}$ plot showing isotopic compositions of ore related carbonate at Au deposits and
957 exploration targets in the Loulo District, in addition to compositional ranges of Kofi Series dolostones
958 and barren carbonate veining. Black curve with open circles represents C-O isotopic compositions
959 expected in carbonates precipitated from a mixture of aqueous-carbonic fluid with a starting
960 composition of $\delta^{18}\text{O} = 10.2 \text{ ‰}$ and $\delta^{13}\text{C} = -27 \text{ ‰}$ and a magmatic fluid with a starting composition of
961 $\delta^{18}\text{O} = 9.4 \text{ ‰}$ and $\delta^{13}\text{C} = -6 \text{ ‰}$ (red star). Black curve with grey circles represents C-O isotopic values
962 expected in carbonates precipitated from a mixture of the same aqueous-carbonic fluid with a brine of
963 meta-evaporite origin and starting isotopic composition of $\delta^{18}\text{O} = 16.2 \text{ ‰}$ and $\delta^{13}\text{C} = -2.6 \text{ ‰}$ (blue star).
964 Red curve represents C-O isotopic fluid values resulting from the magmatic fluid reacting with the Kofi
965 Series dolostones (light grey field; average composition of $\delta^{18}\text{O} = 21 \text{ ‰}$ and $\delta^{13}\text{C} = -0.5 \text{ ‰}$). The curve
966 was modelled at 550 °C XCO_2 of 0.11. Blue, violet, and purple curves represent isotopic compositions
967 resulting from reaction between the aqueous-carbonic fluid and the Kofi dolostones at 295, 325, and
968 400 °C , respectively and at XCO_2 of 0.2. Isotopic compositional ranges for magmatic fluids (red field)

969 (Ohmoto, 1972) and Precambrian marine carbonates (blue field) (Eichmann and Schidlowski, 1975) are
970 given for reference.

971 Fig. 8. Cartoon cross section showing (A) Kofi Series metasedimentary rocks, including evaporite
972 bearing dolostone horizons in the west of the Series, these are folded and metamorphosed prior to 2085
973 Ma, with minor albitisation indicating the presence of early saline brines. (B) Intrusion of the Falémé
974 Batholith from approx. 2085 Ma increases the local geothermal gradient and exsolves magmatic-
975 hydrothermal fluid. This event may both promote devolatilization of the dolostones in the Western Kofi
976 Series and allow water-rock reaction between the magmatic fluids and the evaporite-bearing marly
977 dolostones; this gives rise to a hybridized hypersaline magmatic-evaporitic brine, which circulates
978 through the metasedimentary rocks leading to the development of albitized and tourmalinized rock
979 packages. (C) Between 2085 and 2070 Ma hybrid brines continue to circulate, aqueous-carbonic fluids
980 are introduced along significant structures in the Kofi Series and further magmatism in the Falémé
981 batholith leads to emplacement of small stocks and dikes which extend into the Kofi Series. The
982 aqueous-carbonic fluid unmixes in response to pressure fluctuations, contributing to Au mineralization;
983 at Gara and several other deposits this process is enhanced by partial mixing with hybrid hypersaline
984 brines. Minor amounts of magmatic-hydrothermal fluid derived from dikes cross cutting the Kofi Series
985 may contribute volatiles directly to some of the minor mineralized rock packages in the west of the
986 Loulo Au system. Magnetite skarn deposits simultaneously develop within and adjacent to small dioritic
987 stocks in the Falémé batholith and western Kofi Series.



Gold deposit styles

- Post-collision, orogenic
- Tarkwaian paleoplacer
- skarn
- Post-collision, Loulo/Falémé
- Eburnean basin orogenic
- Eoeburnean orogenic
- Granitoid-hosted
- Eburnean orogenic, part or wholly hosted by Eoeburnian rocks

Gold deposit size

- > 50 Moz
- 8 - 50 Moz
- 3 - 8 Moz
- < 3 Moz

5 km

UTM 29N

N

Legend

Post-Birimian lithologies

 Dolerite

Altered rocks

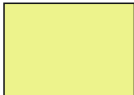
 Intense albitisation

 Strong albitisation (protolith identifiable)

 Iron skarn mineralisation

Igneous lithologies

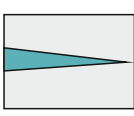
 Faleme batholith plutonic rocks

 Volcaniclastic and sedimentary rocks

 Rhyolitic breccia

Kofi Series

 Marly and variably altered marble

 Sandstones, siltstones, wackes and argillites with polymict conglomerate

 Bedding

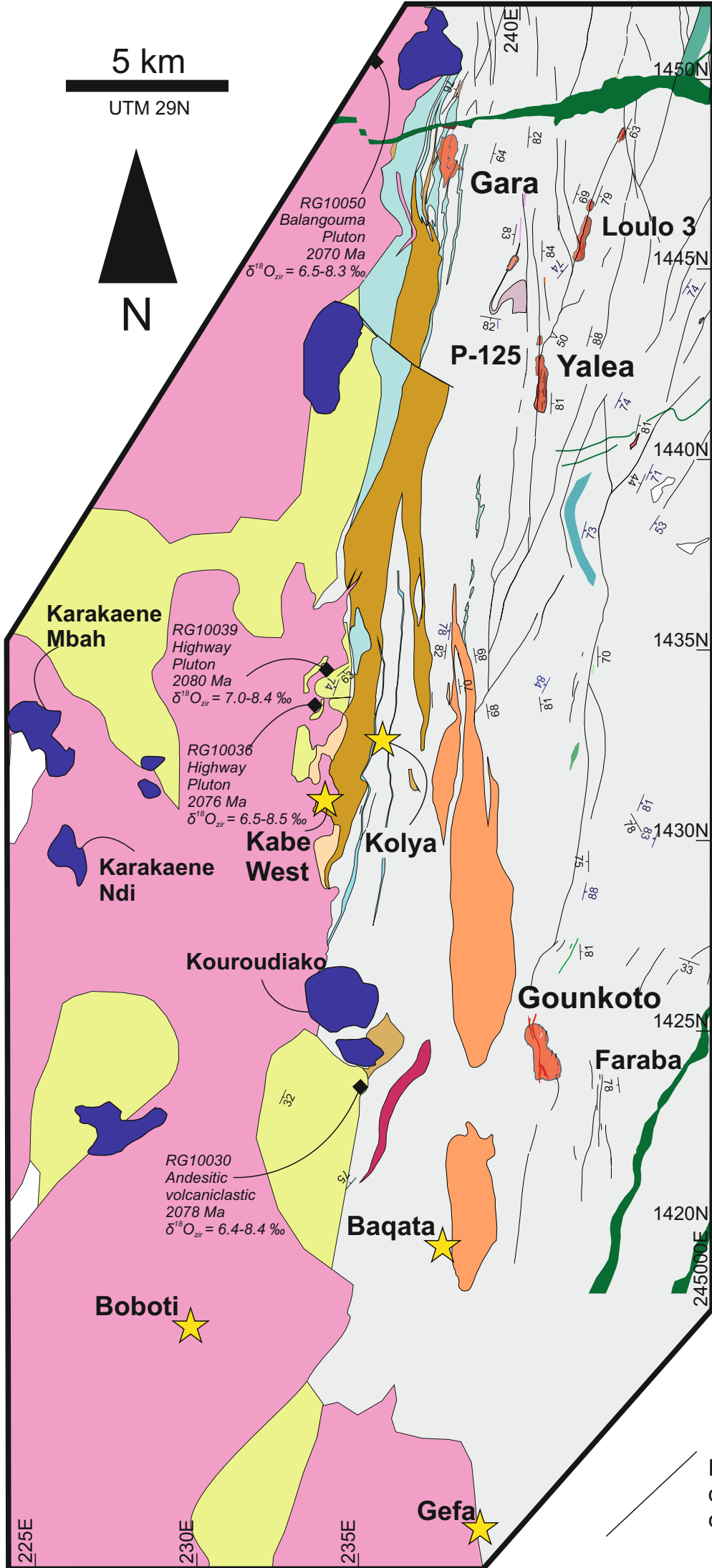
 S_{2L} cleavage

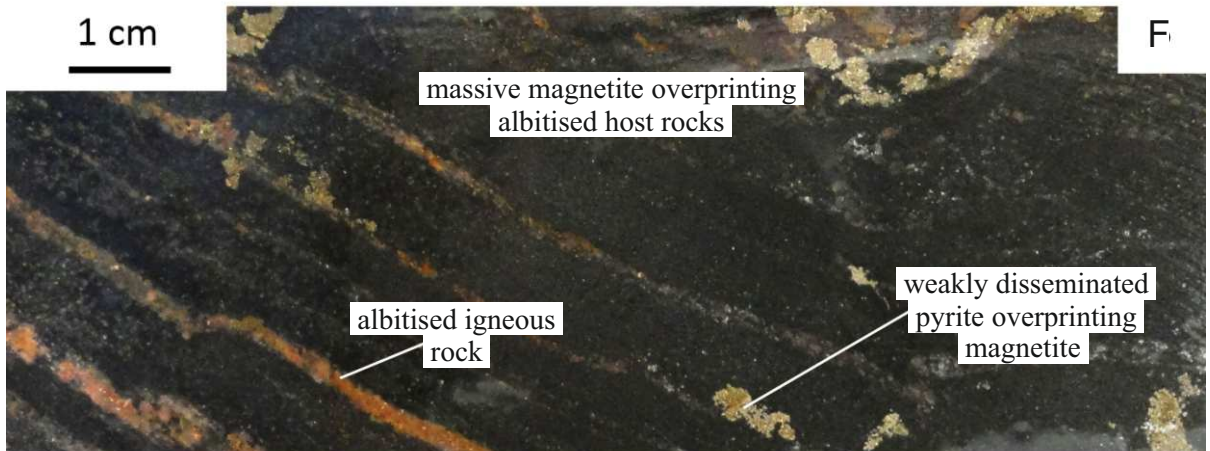
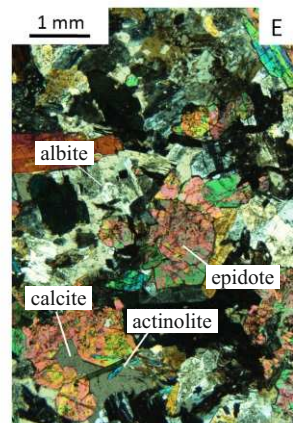
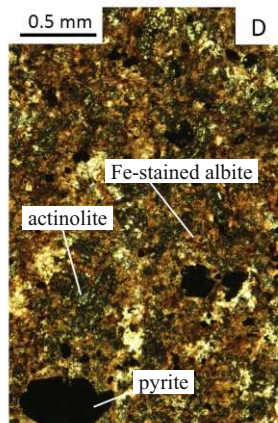
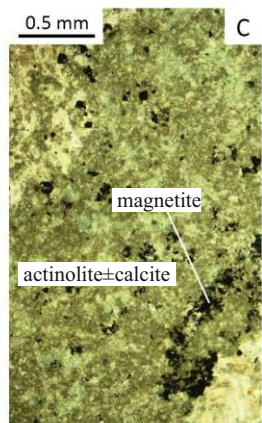
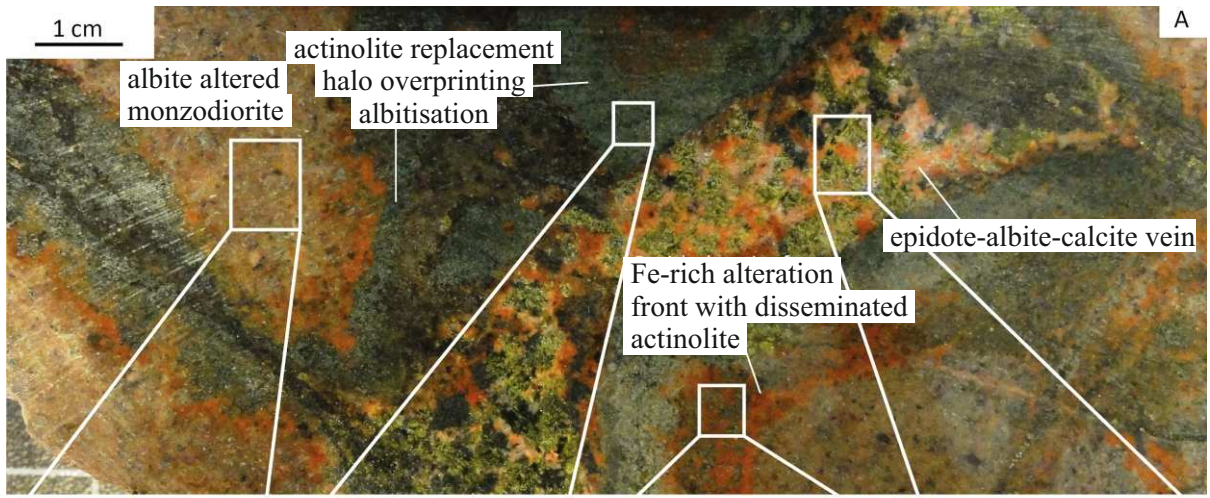
 Magmatic and volcanic rock samples with $\delta^{18}O_{zircon}$ data

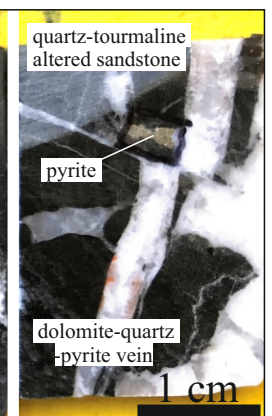
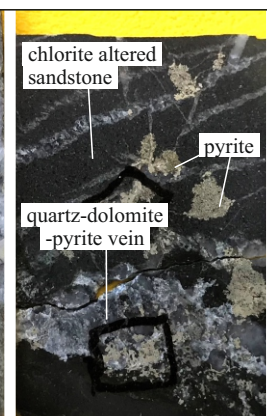
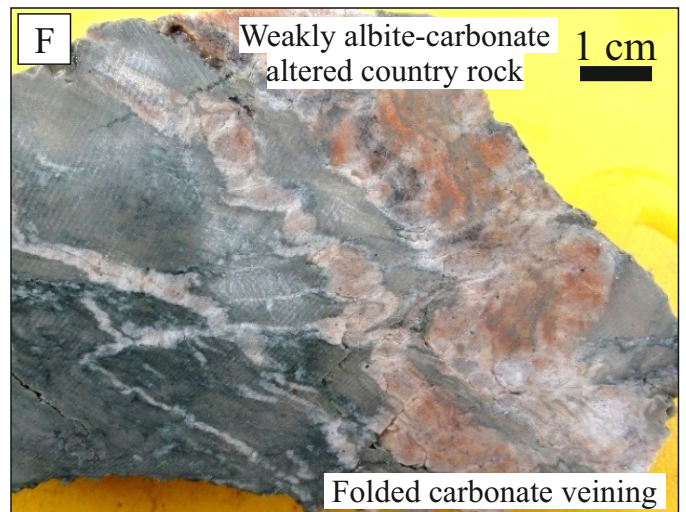
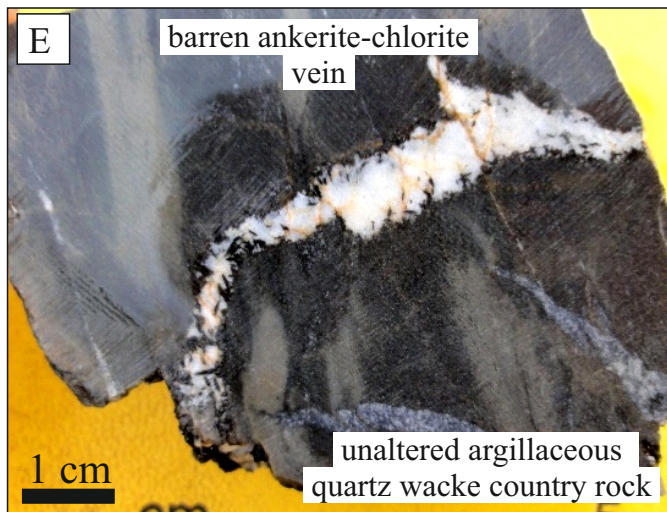
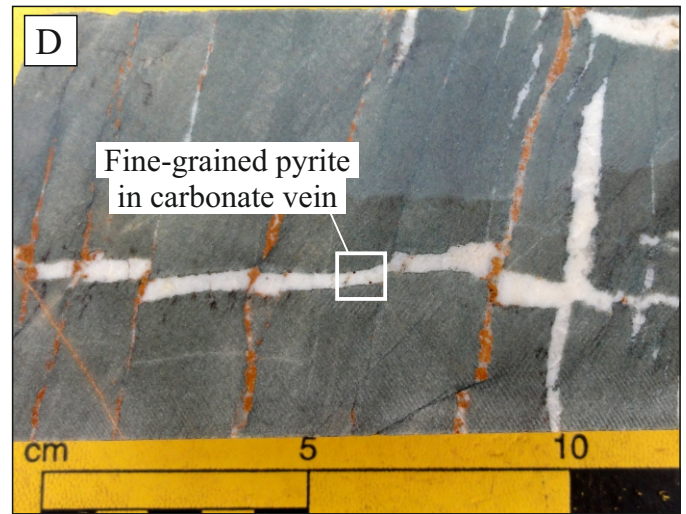
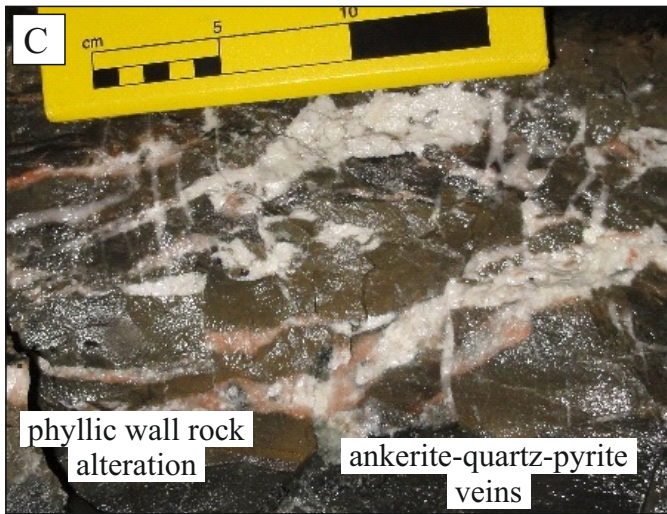
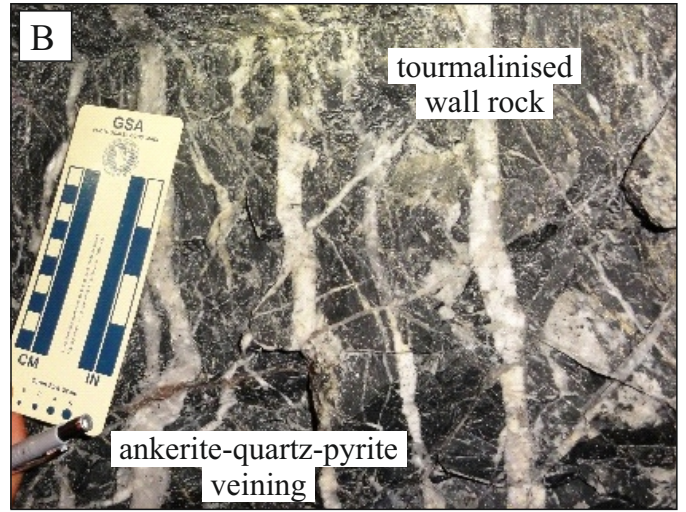
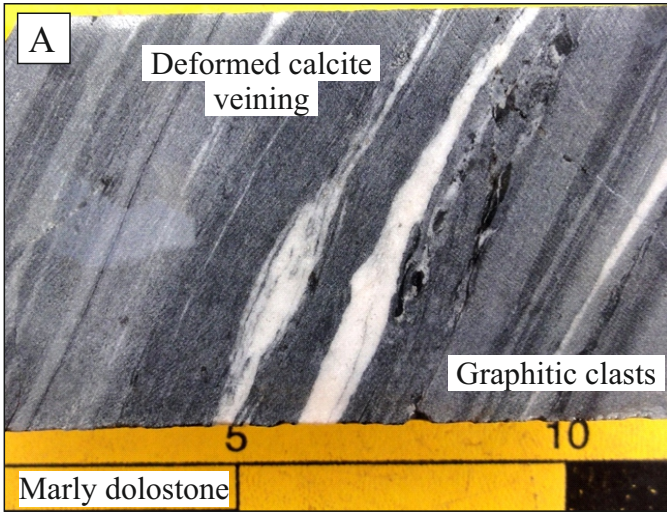
 Exploration targets

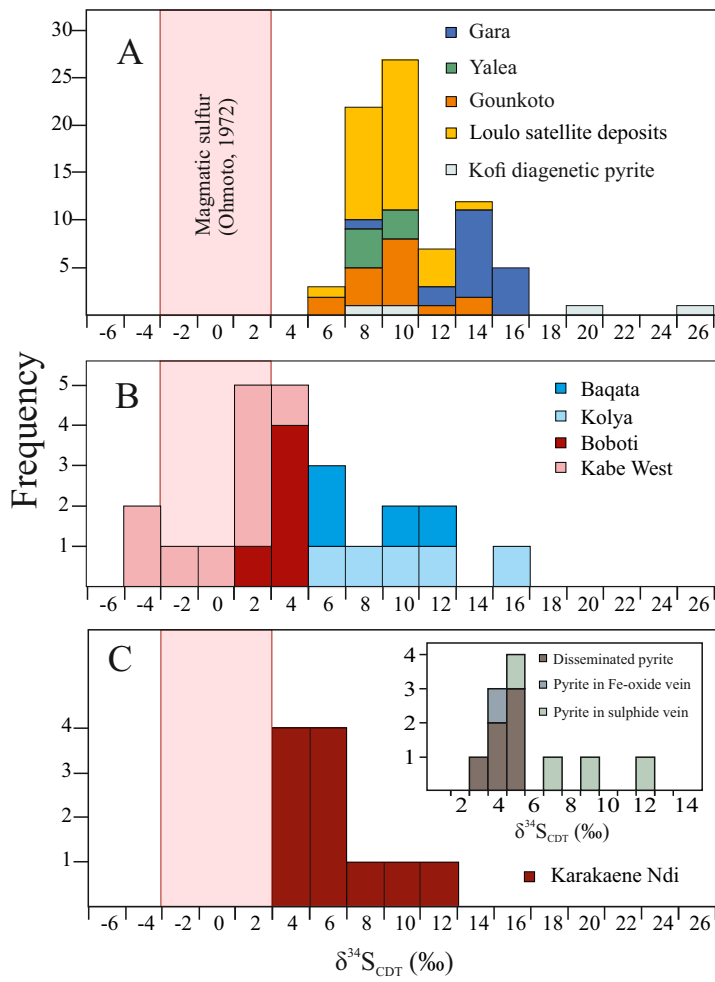
 Au mine

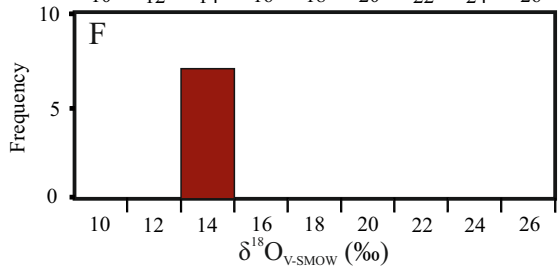
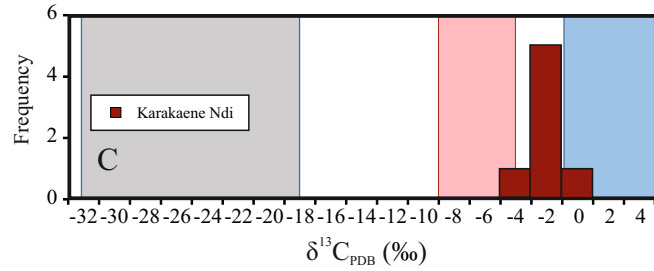
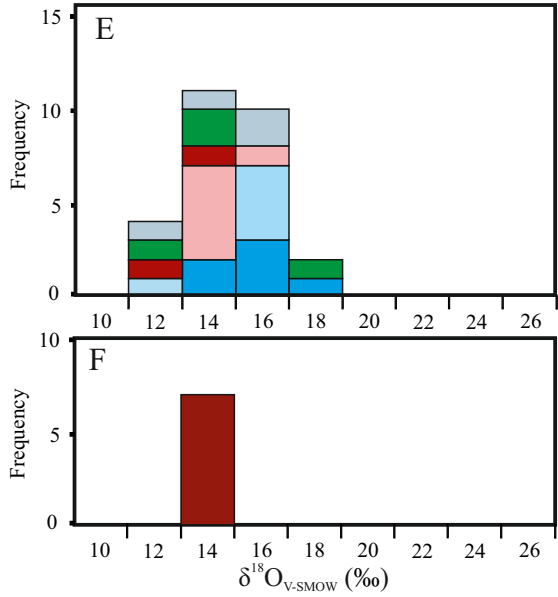
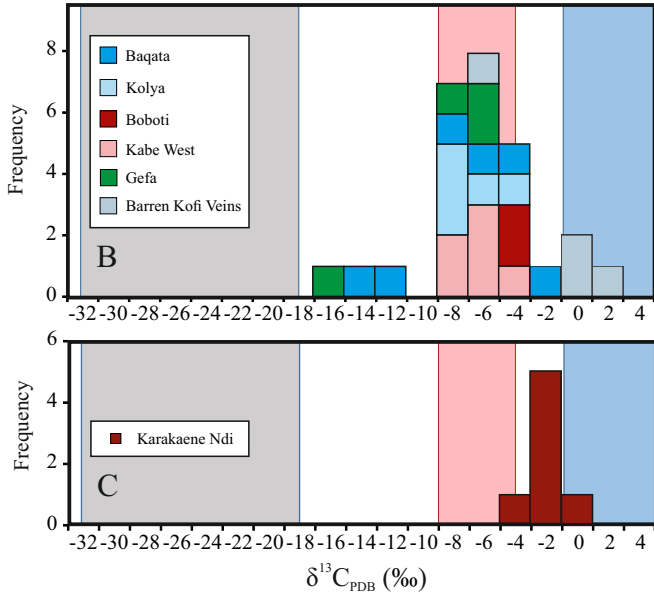
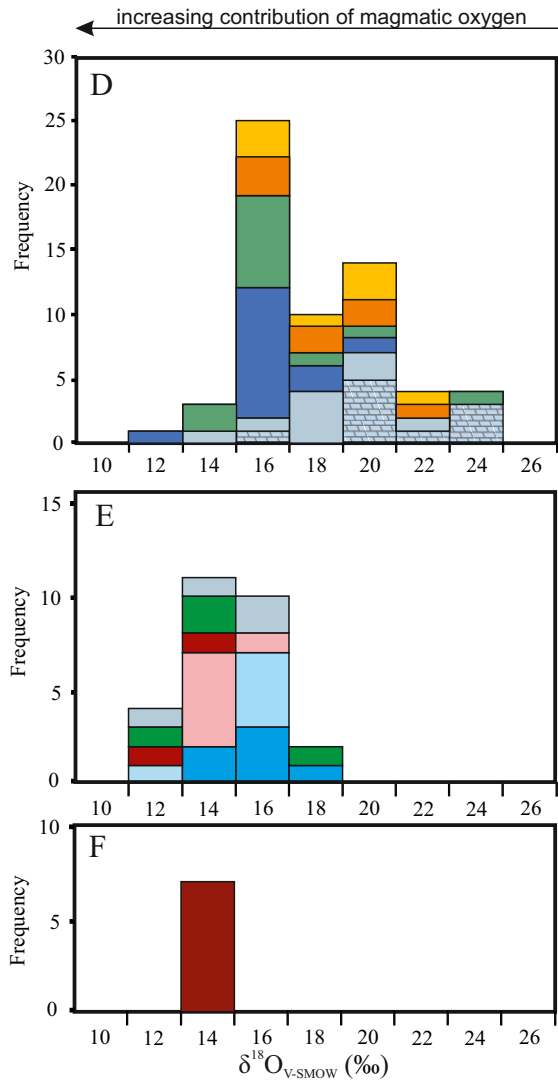
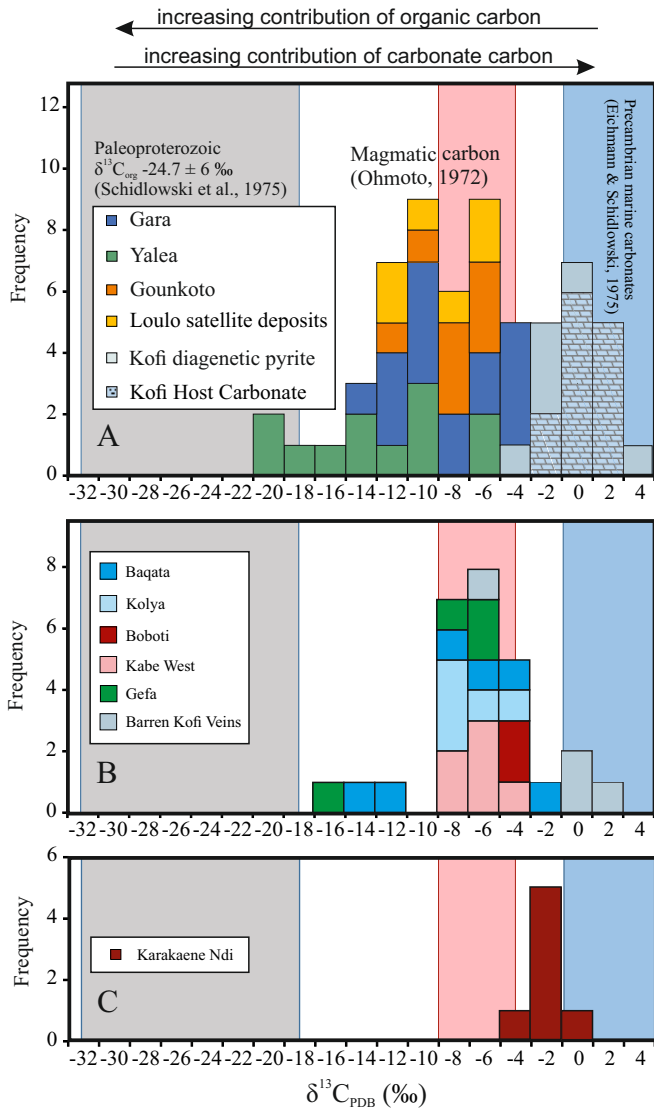
Faults, fractures and shear zones from drilling and outcrop and inferred from chargeability and VTEM data

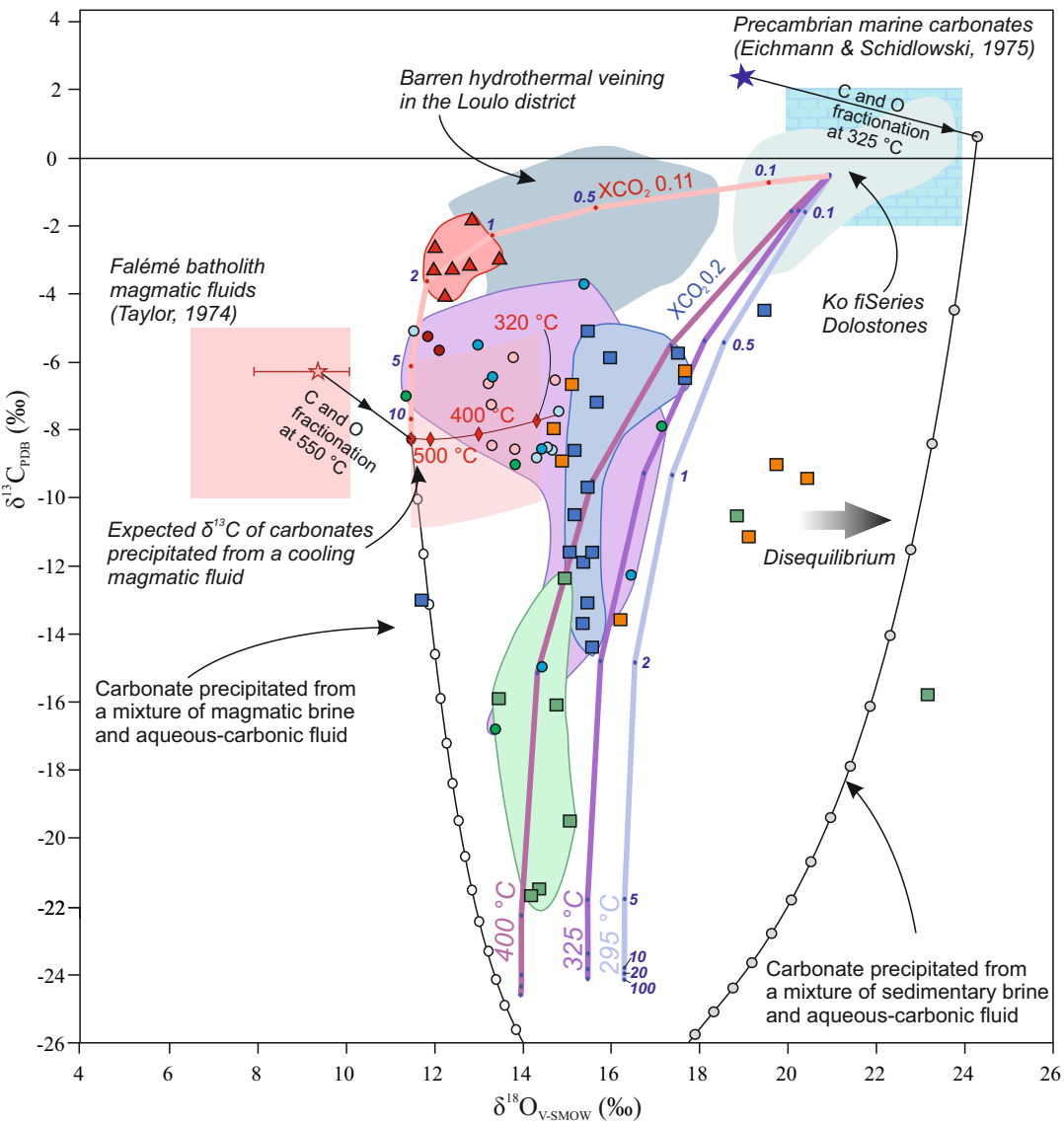












Legend

Deposits >3 Moz

- Gara
- Yalea
- Goukoto

Exploration targets

- Boboti
- Kolya
- Baqata
- Kabe West
- Gefa

▲ Karakaene Ndi Fe skarn

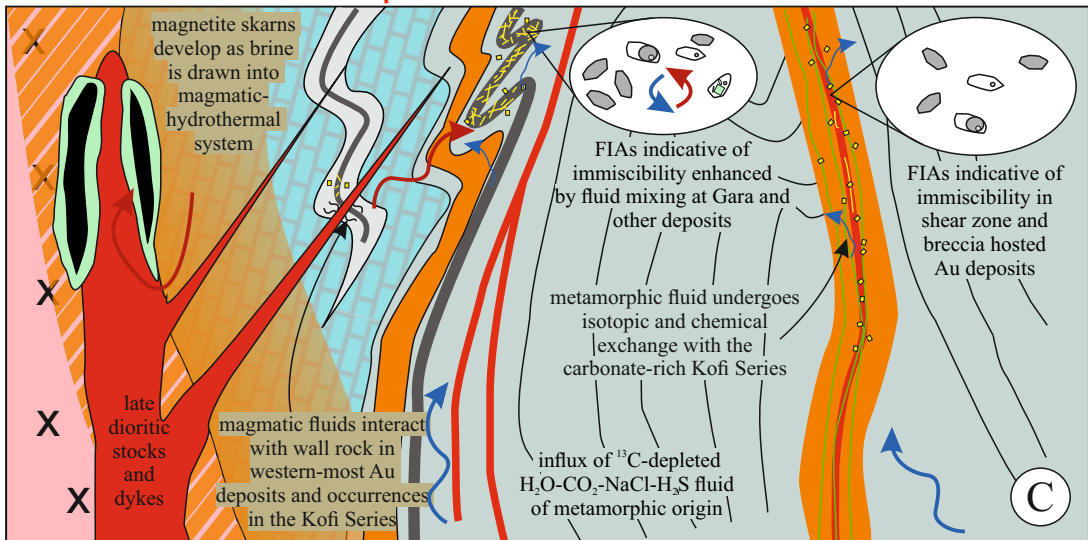
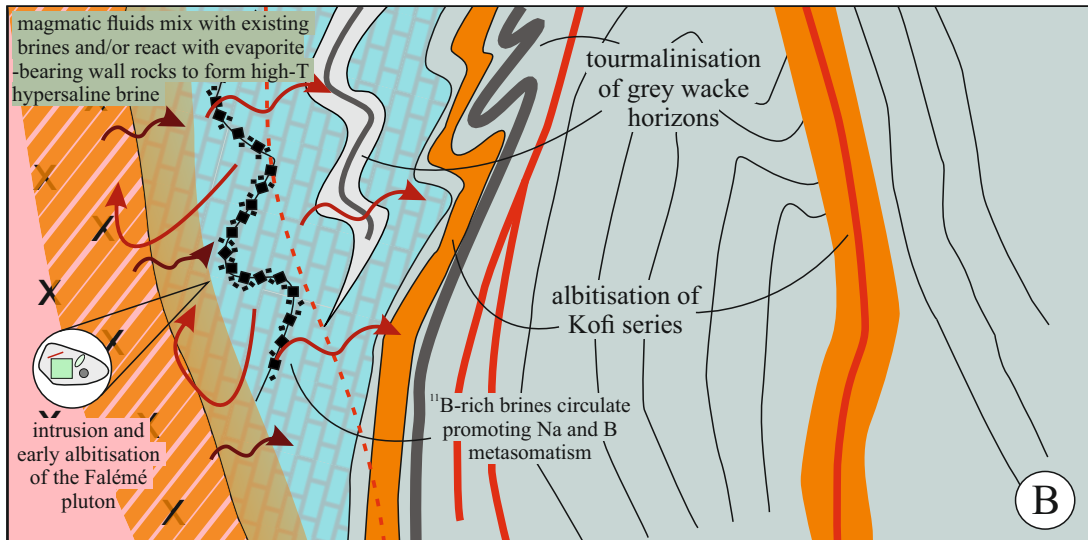
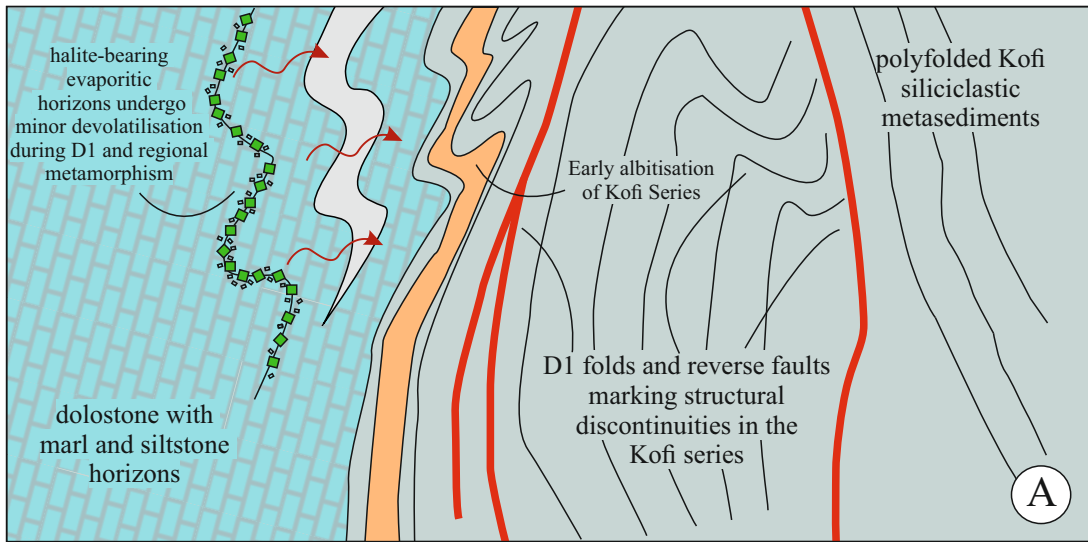
■ Barren veins

■ Kofi dolostones

■ Magmatic fluid range

★ Falémé magmatic fluid

★ Isotopic composition of sedimentary brine



Ore Body	Key ore textures	Ore mineralogy	Alteration styles	P-T conditions	Constraint	Reference
Gold						
Gara	carbonate-quartz-pyrite vein stockwork	pyrite (\pm Ni-Co)-monazite-xenotime-scheelite-gold-chalcopyrite-gersdorffite-pentlandite-Ni-pyrrhotite-arsenopyrite-molybdenite	Tourmalinisation and minor albitisation	>340 °C at 1.75 kbar	Fluid inclusions, O-isotope equilibria, arsenopyrite geothermometry	Lawrence et al. (2013a, b)
Yalea	Shear zone hosted sulphide stringers and hydrothermal breccia	arsenian pyrite-arsenopyrite-chalcopyrite-gold-pyrrhotite-jamesonite-galena-scheelite-tennantite	Early albitisation and syn-mineralisation chloritisation	320 °C at 1.45 Kbar (5.4 km)	Fluid inclusions, arsenopyrite and chlorite geothermometry, O-isotope equilibria	Lawrence et al. (2013a, b)
Goukoto	Shear zone hosted sulphide stringers and hydrothermal breccia	pyrite (\pm As)-arsenopyrite-pyrrhotite-chalcopyrite-magnetite-haematite-gold-monzazite-scheelite-gersdorffite-cobaltite-tennantite-altaite-tellurium-callaverite-sylvanite-petzite	Early albitisation and syn-mineralisation chloritisation - minor tourmalinisation	340 °C at 1.4 Kbar (5.2 km)	Fluid inclusions, arsenopyrite and chlorite geothermometry, O-isotope equilibria	Lambert-Smith et al. (2016b)
Faraba	Quartz-dolomite veining, sulfide-chlorite-magnetite veining and disseminated	arsenian pyrite - arsenopyrite - magnetite-pyrrhotite - chalcopyrite - gold - tsumoite - altaite - hedleyite - bismuth	Early albitisation and syn-mineralisation chloritisation	-		
Sub-economic gold						
Baqata	carbonate-quartz-pyrite vein stockwork and disseminated	pyrite (\pm Ni-As) - chalcopyrite-pyrrhotite-monazite-scheelite-xenotime-gold-millerite-polydymite-sternbergite-tellurobismuthite-calaverite-bismuth	Tourmalinisation and albitisation	\sim 315 °C at 1.3 Kbar (4.8 km)	Fluid inclusions, chlorite geothermometry	Lambert-Smith (2014)
Kolya	carbonate-quartz-pyrite vein stockwork	pyrite - chalcopyrite-arsenian pyrite- scheelite-monazite-xenotime-gold-tellurobismuthite-altaite-melonite	Tourmalinisation and minor actinolite replacement	>300 °C	Fluid inclusions (minimum trapping)	Lambert-Smith (2014)
Kabe West	Hydrothermal breccia - carbonate vein stockwork	pyrite (\pm Ni-Co) - chalcopyrite-monazite-gold-xenotime-altaite-melonite	Albitisation + weak tourmaline	\sim 308 °C	O-isotope equilibria	Lambert-Smith (2014)
Boboti	Hydrothermal veining	pyrite - monazite-gold-haematite-titanite	Weak albitisation	-		
Gefa	carbonate-quartz-pyrite vein stockwork and weakly disseminated	pyrite - chalcopyrite	Tourmalinisation and albitisation	-		
Iron						
Karakaene Ndi	Massive magnetite with late disseminated and vein hosted sulphides	magnetite - haematite - pyrite (N i \pm As substitution)-apatite-chalcopyrite-monazite-gold-uraninite-bismuth-clausenthalite	Early albitisation overprinted by calc-silicate and magnetite replacement	500 °C at 2.5 kbar	Fluid inclusions, O-isotope equilibria	Lambert-Smith (2014)

Deposit / Target	Sample	$\delta^{34}\text{S}(\text{‰ vs. CDT})$	Mineral	Notes	
Host Rock					
Diagenetic pyrite in dolostone	JLSB09	19.70	Pyrite		
	JLSB07	25.10	Pyrite		
	07YD52	9.00	pyrite		
	07YD89	6.40	pyrite		
Target					
Kolya	JLSB08	9.30	Pyrite		
	JLSB29	14.20	Pyrite		
	JLSB30	7.00	Pyrite		
	JLSB31	4.20	Pyrite		
	JLSB06	10.20	Pyrite		
Boboti	JLSB15	2.60	Pyrite		
	JLSB16	2.20	Pyrite		
	JLSB17	3.90	Pyrite		
	JLSB18	1.70	Pyrite		
	JLSB19	2.10	Pyrite		
Baqata	JLSB12	6.00	Pyrite		
	JLSB25	5.50	Pyrite		
	JLSB27	8.90	Pyrite		
	JLSB26	11.80	Pyrite		
	JLSB21	-4.60	Pyrite		
Kabe West	JLSB23	-3.50	Pyrite		
	KBP01	-4.08	Pyrite		
	KBP02	1.06	Pyrite		
	KBP03	1.36	Pyrite		
	KBP05	-0.65	Pyrite		
	KBP11	1.95	Pyrite		
	KBP12	1.82	Pyrite		
	JLSB22	3.40	Pyrite		
	Skarns				
	Karakaene Ndi	JLSB01	4.40	Pyrite	Disseminated
JLSB03		4.20	Pyrite	Disseminated	
JLSB04		3.80	Pyrite	Disseminated	
JLSB05		4.10	Pyrite	Disseminated	
JLSB34 (2)		3.10	Pyrite	Disseminated	
JLSB35		2.80	Pyrite	Disseminated	
JLSB33		4.00	Pyrite	Fe-oxide vein	
JLSB36		7.00	Pyrite	Sulphide vein	
JLSB37		8.07	Pyrite	Sulphide vein	
JLSB38		11.90	Pyrite	Sulphide vein	
JLSB39	4.90	Pyrite	Sulphide vein		
Loulo Au deposits					
Faraba	‡FA20	10.60	Pyrite		
	‡FA04	11.40	Pyrite		
	‡FA10	11.90	Pyrite		
	‡FA23	12.60	Pyrite		
	†PT5	15.20	pyrite		
	†PT6	15.50	pyrite		
	†LD13	14.10	pyrite		

	†LD20	13.60	pyrite
	†LD30	13.80	pyrite
	†LD38	14.50	pyrite
	†LD44	11.70	pyrite
	†LD45	13.30	pyrite
Gara	†LD46	11.50	pyrite
	†LD51	14.30	pyrite
	†LD53	12.50	pyrite
	*C13-100.55	12.10	pyrite
	*C23-26.0	12.90	pyrite
	*C23-198.3b	12.50	pyrite
	*C23-198.55	12.90	pyrite
	*C2-17.75	12.90	pyrite
	†LD54	7.00	Pyrite
	‡JLS01	8.20	Pyrite
	‡JLS02	7.00	Pyrite
	‡JLS03	8.40	Pyrite
	‡JLS05	9.50	Pyrite
	‡LS06	10.00	Pyrite
	‡JLS10 (2)	7.10	Pyrite
	‡JLS12	12.50	Pyrite
Goukoto	‡JLS19	7.00	Pyrite
	‡JLS20	9.70	Pyrite
	‡JLS21	12.80	Pyrite
	‡JLS22	5.90	Pyrite
	‡JLS23	8.00	Pyrite
	‡JLS27	9.60	Pyrite
	‡JLS31	10.30	Pyrite
	‡JLS33	9.70	Pyrite
	‡JLS34	6.25	Pyrite
	*C4-18.20	9.20	pyrite
	*C4-21.00	7.80	pyrite
Loulo-3	*C4-16.00	8.90	pyrite
	*C4-18.20	9.20	pyrite
	*C4-21.00	7.80	pyrite
	*C4-16.00	8.90	pyrite
P125	†PT13	6.70	Pyrite
	*C3-51.9	8.90	pyrite
	*C1-46.0a	9.20	pyrite
	*C1-46.0b	8.70	pyrite
	*C1-46.0c	8.10	pyrite
	*C12-72.4	6.00	pyrite
	*C2-54.9	6.70	pyrite
	*C1-44.0	6.90	pyrite
	*C1-41.5	7.70	pyrite
	*C1-43.9	7.30	pyrite
	*C3-35.6	7.80	pyrite
P-64	*C14-60.85	6.70	pyrite
	*C12-45.3	8.40	pyrite
	*C14.58.8	8.00	pyrite

	*C4-31.75	9.50	pyrite
	*C4-41.95	10.50	pyrite
	*C4-34.5	8.70	pyrite
	*C10-58.0	8.80	pyrite
	*C4-64.5	8.60	pyrite
	*C4-38.2	9.10	pyrite
	*C13-68.0	9.50	pyrite
	*C6-120.7	9.70	pyrite
	*C14-58.8	7.00	pyrite
	†PT18	7.30	pyrite
	†PT20	8.00	pyrite
	†PT26	8.80	pyrite
Yalea	†07YD60	8.30	pyrite
	†07YD65	7.10	pyrite
	†07YD76	7.70	pyrite
	†YD11	9.20	Pyrite

Deposit/target Name	Sample	$\delta^{13}\text{CPDB}$ (‰)	$\delta^{18}\text{OSMOW}$ (‰)	Grade (ppm)	Sample type
Host Rock					
Host Dolostone (Baqata)	JLSB9	-1.44	19.10	<0.01	Host rock
Host Dolostone (Gara)	†G13	1.30	23.20	<0.01	Host rock
	†LD16	-0.40	20.70	<0.01	Host rock
	†LD26	0.10	23.30	<0.01	Host rock
	*C23-26	0.50	22.20	<0.01	Host rock
Host Dolostone (Goukoto)	‡JLS11	-0.25	19.75	<0.01	Host rock
	‡JLS32	-3.13	19.26	<0.01	Host rock
Host Dolostone (Kolya)	JLSB7	1.11	15.07	<0.01	Host rock
Host Dolostone (Yalea)	†07YD52	-2.90	20.00	<0.01	Host rock
	†07YD53	0.40	19.90	<0.01	Host rock
Barren veins					
Baqata	JLSB10	-1.74	15.31	<0.01	Vein
Gara	†G39	-0.20	17.40	<0.01	Vein
	†G40	-1.70	21.10	<0.01	Vein
	*C13-114.7	-2.00	15.10	<0.01	Vein
	*C23-84	3.80	16.90	<0.01	Vein
Goukoto	‡JLS18	-2.35	18.23	<0.01	Vein
	‡JLS29	-0.49	18.18	<0.01	Vein
Kolya	JLSB24	0.22	15.21	<0.01	Vein
Yalea	†07YD90	-1.70	16.40	<0.01	Vein
Loulo Au deposits					
Gara	†PT5	-10.50	15.20	3.36	Vein
Gara	†PT9	-11.90	15.40	86.40	Vein
Gara	†LD13	-13.70	15.40	31.40	Vein
Gara	†LD20	-11.60	15.60	90.30	Vein
Gara	†LD31	-13.10	15.50	6.20	Vein
Gara	†LD32	-9.70	15.50	27.80	Vein
Gara	†LD44	-14.40	15.60	8.20	Vein
Gara	†LD45	-11.60	15.10	4.65	Vein
Gara	†LD46	-8.60	15.20	26.80	Vein
Gara	*C13-100.55	-5.90	16.00	-	Vein
Gara	*C23-198.3a	-6.50	17.70	-	Vein
Gara	*C23-198.3b	-4.50	19.50	-	Vein
Gara	*C14-112.5	-5.10	15.50	-	Vein
Gara	*C6-41	-7.20	15.70	-	Vein
Goukoto	‡JLS06	-11.15	19.15	35.10	Vein
Goukoto	‡JLS12	-13.60	16.25	7.80	Vein
Goukoto	‡JLS25	-6.30	17.71	-	Vein
Goukoto	‡JLS26	-9.44	20.47	-	Vein
Goukoto	‡JLS28	-6.68	15.16	<0.01	Vein
Goukoto	‡JLS33	-8.93	14.92	2.90	Vein
Goukoto	‡JLS34	-9.03	19.77	0.26	Vein
Goukoto	‡JLS35	-7.99	14.73	0.04	Vein
Yalea Main	†07YD69	-15.80	23.20	15.98	Vein
Yalea Main	†08YD10	-19.50	15.10	-	Vein
Yalea Main	†07YD71	-21.50	14.40	9.43	Wall rock alteration
Yalea Main	†07YD76	-21.70	14.20	5.51	Wall rock alteration
Yalea Main	†08YD24	-15.90	13.50	5.51	Wall rock alteration
Yalea Main	†08YD33	-16.10	14.80	7.80	Wall rock alteration
Faraba	FA20	-6.63	15.42	4.57	Vein
Faraba	FA6	-13.20	20.50	0.34	Vein
Faraba	FA7	-12.20	18.20	0.45	Vein
Faraba	FA12	-10.90	18.50	4.98	Vein

P-64	*C2-52	-7.00	16.90	-	Vein
P-64	*C4-75.5	-8.50	19.10	-	Vein
Target					
Baqata	JLSB11	-3.74	15.42	<0.01	Vein
Baqata	JLSB26	-14.97	14.47	0.13	Vein
Baqata	JLSB28	-8.58	14.46	<0.01	Vein
Baqata	JLSBP10	-6.46	13.35	<0.01	Vein
Baqata	JLSBP12	-5.53	13.03	<0.01	Vein
Baqata	JLSBP17	-12.28	16.48	<0.01	Vein
Boboti	JLSB17	-5.27	11.88	0.04	Vein
Boboti	JLSB18	-5.68	12.15	<0.01	Vein
Gefa	JLSBP44	-16.80	13.41	0.01	Vein
Gefa	JLSBP46	-7.92	17.18	0.01	Vein
Gefa	JLSBP51	-7.02	11.39	0.01	Vein
Gefa	JLSBP55	-9.03	13.86	0.01	Vein
Kabe West	JLSB21	-7.27	13.32	11.53	Vein
Kabe West	JLSB22	-8.47	13.34	0.56	Vein
Kabe West	KBP01	-6.55	14.77	11.33	Vein
Kabe West	KBP03	-5.88	13.82	2.05	Vein
Kabe West	KBP06	-8.58	13.85	0.20	Vein
Kabe West	KBP12	-6.66	13.25	0.01	Vein
Kolya	JLSB29	-7.47	14.85	0.39	Vein
Kolya	JLSB30	-8.84	14.35	0.16	Vein
Kolya	JLSB31	-8.52	14.58	0.08	Vein
Kolya	JLSB32	-8.60	14.69	0.60	Vein

	wt. % NaCl equiv.	X _{H2O}	X _{NaCl}	X _{CO2}	m _{H2O}	m _{NaCl}	m _{CO2}	δ ¹³ C _i (‰)	δ ¹⁸ O _i (‰)
Kofi Series evaporite brine	41.70	0.70	0.25	0.05	38.86	4.28	1.14	1.80	17.25
Metamorphic fluid	6.10	0.78	0.02	0.20	43.19	0.38	4.54	-27.00	10.20
Magmatic Fluid	3.30	0.82	0.02	0.16	45.67	0.30	3.64	-6.00	9.40

3.5E+08